Petroleum Science 23 (2026) 2086–2105

Contents lists available at ScienceDirect

Petroleum Science

journal homepage: www.keaipublishing.com/en/journals/petroleum-science

Original Paper

Multi-component composite steam flooding (MCCSF) expanding steam chamber and suppressing water invasion in edge-water heavy oil reservoirs: A comparative 3D experimental study

Qing-Jing Hong [a], Zhan-Xi Pang [a,*], Peng Tang [a], Xiao-Hong Liu [b], Bo Wang [c]

[a] State Key Laboratory of Petroleum Resources and Engineering, China University of Petroleum (Beijing), Beijing, 102249, China
[b] Tianjin Branch of China National Offshore Oil Company (CNOOC) Ltd., Tianjin, 300452, China
[c] Henan Oilfield Institute, Sinopec China, Nanyang, 473400, Henan, China

ARTICLE INFO

Article history:
Received 14 August 2025
Received in revised form
13 January 2026
Accepted 13 January 2026
Available online 21 January 2026

Edited by Yan-Hua Sun

Keywords:
Edge-water
Steam flooding
3D experiments
Multi-component
Steam chamber
Image recognition
EOR mechanisms

ABSTRACT

The development of heavy oil reservoirs with edge-water presents significant challenges during pure steam flooding (PSF), including steam override, severe channeling, limited displacement/sweep efficiency, and water invasion. To address these issues, multi-component composite steam flooding (MCCSF) was proposed as an improved steam flooding (SF) method. This study introduced a novel three-dimensional (3D) physical simulation approach that accurately replicated the recovery process in edge-water reservoirs. Additionally, a new similarity criterion number was proposed to characterize edge-water energy conversion. Then, comparative experiments (Exp. A: PSF; Exp. B: MCCSF) were conducted to elucidate the advantages and enhanced oil recovery (EOR) mechanisms of MCCSF. Results demonstrated that MCCSF effectively accelerated the thermal connection between wells, mitigated steam override, and improved steam thermal utilization. Compared with PSF, MCCSF achieved higher peak oil production rate and longer stable production stage. In heterogeneous reservoirs with structural dip, MCCSF generated a more uniform steam chamber and reduced the performance gap between higher and lower wells. Post-displacement oil saturation in the middle and upper main layers was typically 7%–10% lower under MCCSF than under PSF. Furthermore, MCCSF significantly suppressed the degree and extent of edge-water invasion in the lower reservoir zones. The final oil recovery factor of MCCSF reached 55.37%, representing an 11.71% improvement over PSF. This study established a scalable laboratory methodology and revealed the coupled displacement mechanisms of steam–gas–chemical system under edge-water conditions, offering both theoretical insights and experimental support for optimizing thermal recovery in heavy oil reservoirs.

1. Introduction

Heavy oil represents a globally prevalent unconventional resource whose development gains increasing importance as recoverable light oil reserves decline (Guo et al., 2016; Elahi et al., 2019). Distinguished from conventional petroleum by high viscosity, elevated asphaltene content, significant burial depth, and limited mobility under reservoir conditions, it required specialized recovery methods beyond conventional approaches (Jiang et al., 2025; Zhang et al., 2025). Thermal techniques—notably steam huff and puff (SHP), steam flooding (SF), steam-assisted gravity drainage (SAGD), and in-situ combustion—remained dominant for heavy oil development (Jayasekera and Goodyear, 2000; Sun et al., 2023). Where SHP and SF are the most widely used among them. Following SHP preheating, SF typically served as the follow-up process (Pang et al., 2024; Dang et al., 2025). Optimizing recovery of SF stage while reducing costs thus presented a critical challenge in heavy oil exploitation, especially in the development of complex reservoirs, such as the presence of edge-water in the reservoir (Sun et al., 2017; Dong et al., 2019; Li et al., 2025). During SF processes, severe fingering and channeling reduced steam circulation and sweep efficiency. Steam override further decreased thermal efficiency and raised operational costs, which makes it

* Corresponding author.
E-mail address: pxiad9827@163.com (Z.-X. Pang).
Peer review under the responsibility of China University of Petroleum (Beijing).

https://doi.org/10.1016/j.petsci.2026.01.018

Nomenclature

a	Edge-water multiplier, dimensionless
B	Formation thermal conductivity, kJ/(m·s·K)
C_f	Compressibility of rock, MPa^{-1}
C_g	Compressibility of gas, MPa^{-1}
C_L	Compressibility of liquid, MPa^{-1}
C_o	Compressibility of oil, MPa^{-1}
C_w	Compressibility of water, MPa^{-1}
g	Acceleration of gravity, m/s^2
H	Net pay, m
i_s	Gas injection rate, m^3/d
i	i-th layer of the oil sand-pack external aquifer, dimensionless
j	j-th layer of the water sand-pack external aquifer, dimensionless
k	k-th layer of the external aquifer, dimensionless
K	Permeability, μm^2
L	Well length, m
L_1	Width of the 3D model, cm
L_2	Internal oil–water boundary distance after conversion, cm
L_3	External oil–water boundary distance after conversion, cm
m	Number of oil sand-packs, dimensionless
M_o	Heat capacity of oil, $kJ/(m^3·K)$
M_{ro}	Heat capacity of oil layer, $kJ/(m^3·K)$
M_{rw}	Heat capacity of water layer, $kJ/(m^3·K)$
M_w	Heat capacity of water, $kJ/(m^3·K)$
n	Number of sand-packs, dimensionless
p_1	Pressure after completion of displacement, MPa
p_r	Initial reservoir pressure, MPa
Re	Reynolds number, dimensionless
S_o	Oil saturation, dimensionless
S_{oa}	Average oil saturation of the selected area, dimensionless
S_{oi}	Oil saturation corresponding to a specific pixel, dimensionless
S_w	Water saturation, dimensionless
t	Time, min
T	Temperature, °C
u	Number of pixels in the selected area, dimensionless
ν_t	Seepage velocity, m/s
V_{gi}	Volume of gas tank of the i-th oil sand-pack, L
V_{gj}	Volume of gas tank of the j-th water sand-pack, L
V_{gn}	n-th layer external gas tank volume, cm^3
V_{L1}	Elastic productivity under reservoir conditions, m^3
V_{L2}	Elastic productivity under experimental conditions, m^3
V_{model}	Volume of porous media filled in the 3D model, m^3
V_o	Totally geological reserves, m^3
V_{pack}	Volume of sand-pack, m^3
V_r	Gross volume of porous media, m^3
V_{r1}	Volume of oil-bearing porous medium, m^3
V_S	Unreplaced fluid expansion quantity, cm^3
V_{wi}	Volume of water tank of the i-th oil sand-pack, L
V_{wj}	Volume of water tank of the j-th water sand-pack, L
x	Volumetric ratio of water tank to gas tank per layer, dimensionless
y_k	Volumetric ratio of the k-th gas tank to the n-th gas tank, dimensionless
Z	Gas compressibility factor, dimensionless
Δp	Production pressure differential, MPa
ΔS	Mobile oil saturation, dimensionless
ϕ	Porosity, dimensionless
λ	Constraint coefficient, dimensionless
μ_f	Viscosity of fluid, mPa·s
μ_o	Viscosity of experimental oil, mPa·s
ρ_f	Fluid density, kg/m^3
ρ_o	Oil density, kg/m^3

difficult to substantially enhance oil recovery based on SHP (Zhao et al., 2013; Bao et al., 2016; Mahood et al., 2016). Recent research demonstrated that augmenting steam with non-condensable gases (NCG) and chemical additives significantly improved displacement efficiency compared to PSF (Dong, 2012; Afra et al., 2018; Xi et al., 2019; Pratama et al., 2022). This composite approach achieved synergistic multiphase displacement through integrated steam-gas-chemical system, transitioning recovery mechanisms from purely thermal to thermal-plus that enhanced ultimate recovery (Dong et al., 2014; Perez-Perez et al., 2016; Jiang et al., 2024).

Currently, the predominant gaseous composite components employed are NCG, primarily including CO_2, N_2, flue gas, and hydrocarbon gases (Yang et al., 2015). Wang et al. (2025) demonstrated that NCG accumulation at steam chamber peripheries regulated heat distribution and chamber morphology, enhancing oil recovery. CO_2 exhibited superior solvent effects and viscosity reduction capabilities among NCGs. Lin et al. (2025) and Dong et al. (2015) reported that N_2/CO_2-based multi-thermal fluids under equivalent thermal input generated steam chambers 4 times larger than pure steam, while improving displacement efficiency by 10%–25%. Li et al. (2011) and Zou et al. (2025) further established CO_2's exceptional solubility and viscosity reduction under high-pressure/high-temperature reservoir conditions, whereas nitrogen demonstrated negligible solubility in heavy oil with minimal viscosity impact—functioning primarily as a pressure-maintenance agent. Lu et al. (2022) confirmed that flue gas co-injection substantially expanded steam chamber dimensions, yielding significant recovery enhancement. When combined with foaming agents, NCG form foams that deliver dual-enhancement mechanisms: selective plugging of high-permeability channels and enhanced microscopic oil displacement (Chen et al., 2023). Wei et al. (2024) and Lu et al. (2024) demonstrated that CO_2 foams provided synergistic profile control and displacement during SF, improving thermal conformance while expanding frontal coverage. Soomro (2025) revealed that nitrogen foams exhibited superior stability to CO_2 foams in porous media through X-ray computed tomography analysis. Jiang et al. (2021) further developed an alkali-free viscoelastic nitrogen foam system, achieving 22.95% incremental oil recovery compared to surfactant flooding. Viscosity reducer (VR) and organic solvents represent another prevalent composite formulation. McAuliffe (1973) found that emulsions formed by VR and crude oil plugged larger pore throats, redirecting fluid flow to smaller pores, which moderately reduced remaining oil saturation and enhanced sweep efficiency. Pang et al. (2023) showed that solvent–steam co-injection reduced oil viscosity and improved steam chamber propagation, significantly increasing heavy oil recovery. Kar and Hascakir (2021) compared seven solvents in steam-assisted processes, finding that hydrocarbon solvents, particularly n-hexane, enhanced recovery by

reducing water–asphaltene polar interactions and emulsion complexity.

3D experiment provided a scaled experimental methodology that replicated field-scale production dynamics at laboratory dimensions, extensively employed to investigate steam chamber evolution, production performance variations, and EOR mechanisms during thermal recovery. Dong et al. (2022b) utilized this approach to demonstrate that multilateral well SAGD in heavy oil reservoirs shifted steam chamber geometry from an inverted triangle to an inverted trapezoid compared to dual-horizontal well SAGD, increasing recovery efficiency by over 15%. Pang et al. (2021, 2023) applied 3D physical modeling to characterize water invasion behavior during SF in bottom-water heavy oil reservoirs and confirmed that solvent–steam co-injection significantly expanded steam chambers and improved recovery even with bottom-water communication. She et al. (2021) found that higher crude acid number (TAN) and injection velocity promoted emulsification in alkaline flooding through 3D experiments, enhancing oil droplet shearing-entrainment synergy in porous media and boosting recovery in high-TAN reservoirs. Tian et al. (2017) established distinct advantages of low-pressure SAGD operation over high-pressure conditions by 3D experiments, recommending reservoir pressure reduction prior to implementation SAGD in high-pressure heavy oil system.

In this study, we proposed an innovative physical simulation approach incorporating multiple external aquifers. This method eliminated the need for embedded aquifer within 3D models while accurately replicating recovery performance in edge-water reservoirs. Then, we derived a similarity criterion number to characterize edge-water energy conversion during 3D physical experiments. By integrating image recognition algorithms and theoretically edge-water invasion identification methods, we designed two sets of 3D experiments which are PSF and MCCSF. Through comprehensive evaluation of production performance, lateral/horizontal steam chamber development, quantitative analysis of remaining oil by layer and region, and assessment of edge-water invasion, we deeply analyzed the advantages of MCCSF in developing edge-water heavy oil reservoirs compared with PSF and its EOR mechanisms.

2. Simulation method of edge aquifer

In our previous studies, external water and gas tanks were used to simplistically simulate aquifer (Wang et al., 2018; Pang et al., 2021). However, this method is better suited to simulate bottom-water reservoirs, where the oil–water interface is relatively simple and can largely be approximated as a plane parallel to the aquifer. In contrast, edge-water reservoirs exhibit more complex oil–water interface geometries. Additionally, these methods necessitate embedding an aquifer within the 3D model that proves operationally challenging for edge-water reservoirs with structural dip. Furthermore, during field production, side wells keep a certain distance from the edge-water (termed the internal oil–water boundary). Embedding an aquifer in the 3D model artificially reduces the distance between side wells and edge-water, failing to preserve actual well patterns and the true spatial relationship to the aquifer. Crucially, the simplistic coupling of gas and water tanks cannot accurately simulate the oil layer and aquifer outside the simulation range of the 3D model. To address these limitations, we developed an innovative 3D physical simulation methodology for edge-water reservoirs. This method accurately replicated both the complex oil–water interface and the oil/water layer outside the simulation range of the 3D model without the need for an embedded aquifer in the 3D model.

As shown in Fig. 1, the edge-water reservoir geometry was firstly simplified into the polygon combination. The resulting 3D model (illustrated in Fig. 2) excluded any internal aquifer, representing solely the well group area. Surrounding aquifers were instead simulated using sand-pack–tank assemblies. A critical aspect of this method involved determining the appropriate volumes for the water and gas tanks assigned to each aquifer layer. Based on elastic fluid dynamic drive theory, we derived the required volumes for the water and gas tanks in each layer. This derivation simultaneously established a novel similarity criterion number (Eq. (1)) specifically for edge-water energy conversion in 3D experiments. The detailed derivation process was provided in the appendix.

$$\frac{V_s}{V_{gn}} = \sum_{k=1}^{n} y_k \left(x C_w + \frac{1}{p_r} \right) \tag{1}$$

In the study of heavy oil thermal recovery, Pang et al. (2019, 2020, 2021) and Dong et al. (2015, 2022a, 2024) conducted extensive 3D physical simulation experiments and improved the similarity criteria for such experiments. Building on this foundation, by adding the newly derived similarity criterion number for edge-water energy conversion, the similarity criterion for steam flooding under edge-water conditions has been supplemented. The parameters of this similarity criterion were summarized in Table 1.

3. 3D physical simulation

To systematically investigate the impact of injected components on SF performance, two 3D physical simulation experiments were conducted, including a group of SHP converted to PSF (Exp. A), and a group of SHP converted to MCCSF (Exp. B).

3.1. Experimental apparatus

The 3D experimental apparatus (as shown in Fig. 3.) comprised an injection system, a 3D model, an edge-water simulation module, and a collection system. The injection system integrated two ISCO pumps, a steam generator, NCG cylinders, mass flow controllers, liquid tanks, and heating belts. It delivered a maximum steam injection rate of 50 mL/min with 100% quality at 350 °C, and NCG flow rated up to 1000 mL/min. The 3D model is a stainless-steel cube (42 cm × 42 cm × 40 cm) capable of simulating various well types and reservoir thicknesses under conditions up to 20 MPa and 350 °C. It was housed within a thermotank to maintain reservoir temperature and minimize heat loss. The edge-water simulation module adopted an innovative method that used sand-packs, liquid tanks, and gas tanks to replicate edge-water reservoir conditions (as shown in Fig. 2). The collection system included a computer-controlled data acquisition unit, temperature/pressure sensors, a back-pressure valve, and volumetric cylinders. It enabled real-time monitoring of temperature/pressure and accurate fluid metering. Heating belts were applied to the injection line and well ends to maintain steam temperature/quality and prevent cold oil blockage at the production end.

3.2. 3D model structure

Fig. 4 illustrates the model's internal structure and the planar/vertical placement of temperature sensors. Three horizontal wells were positioned in the upper third of the reservoir, including one injection well in the center and two production wells on either side. Four rows of temperature sensors (20 per row) were installed: the first near the top, the second at the well layer, the third in the lower-middle, and the fourth near the bottom of the reservoir. This layout enabled comprehensive planar and vertical temperature profiling.

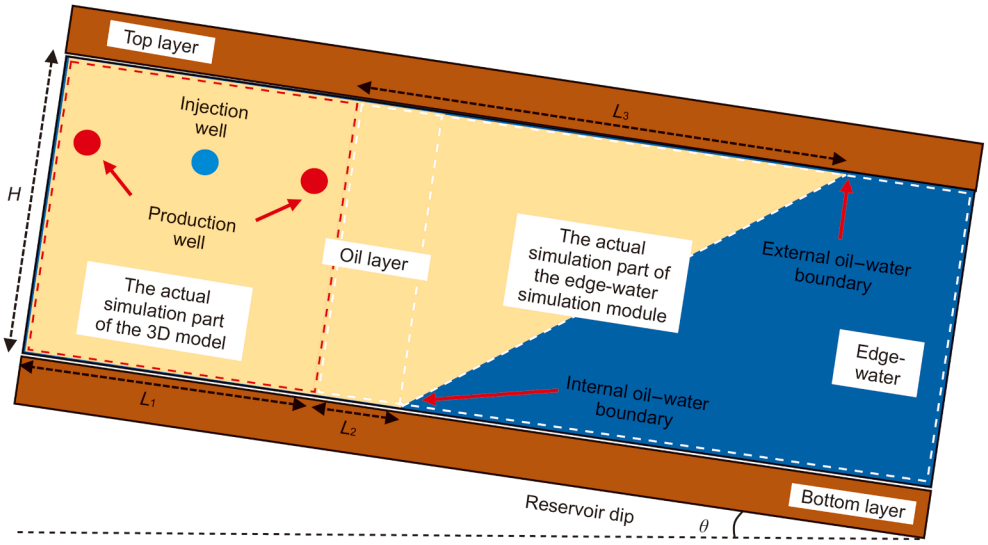

Fig. 1. Simplified equivalent diagram of edge-water reservoir.

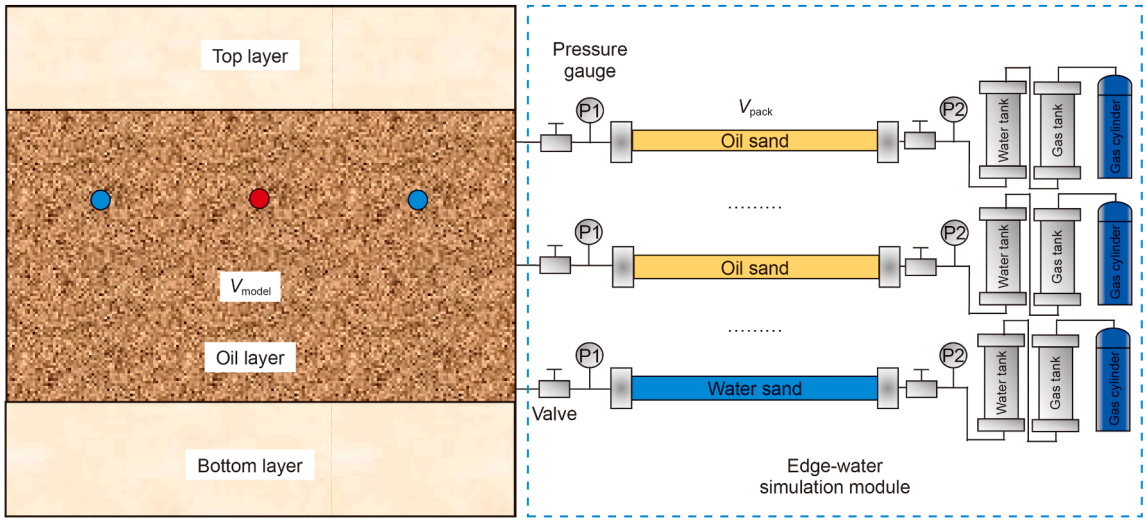

Fig. 2. Schematic of the multiple external aquifer module.

Table 1
The similarity criteria of steam flooding in edge-water reservoir.

Similarity	Physical significance	Simulation parameter
$\pi_1 = \frac{K\rho_o g t}{\phi \Delta S \mu_o L}$	The ratio between gravity and viscous force	Absolute permeability and time
$Re = \frac{K\rho_f^2 L_1 g}{\mu_f^2}$	Reynolds number	Permeability correction
$\pi_2 = \frac{i_s t}{\phi \Delta S \rho_w L^3}$	The mass ratio between steam injection and mobile oil	Steam injection flux
$\pi_3 = \frac{\Delta p}{\rho_o g L}$	The ratio between pressure difference and gravity	Pressure difference
$\frac{V_s}{V_{gn}} = \sum_{k=1}^{n} y_k \left(x C_w + \frac{1}{p_r} \right)$	Elastic energy of edge-water	External gas volume

3.3. Experimental parameters and samples

Actual reservoir conditions: The experimental simulation targeted a specific edge-water heavy oil reservoir in China. The original reservoir temperature and pressure were 54 °C and 12.0 MPa, respectively. The reservoir had an absolute permeability of 0.5–2.0 μm^2, along with a porosity of 0.3, a net pay of 48 m, and a dip angle of 6°. Basic properties of formation water and oil were listed in Table 2. At reservoir temperature, the oil viscosity was 2908 mPa·s, indicating poor mobility. As the temperature increased from 54 to 150 °C, the viscosity significantly decreased to 35 mPa·s, and further dropped to 11 mPa·s at 200 °C. The

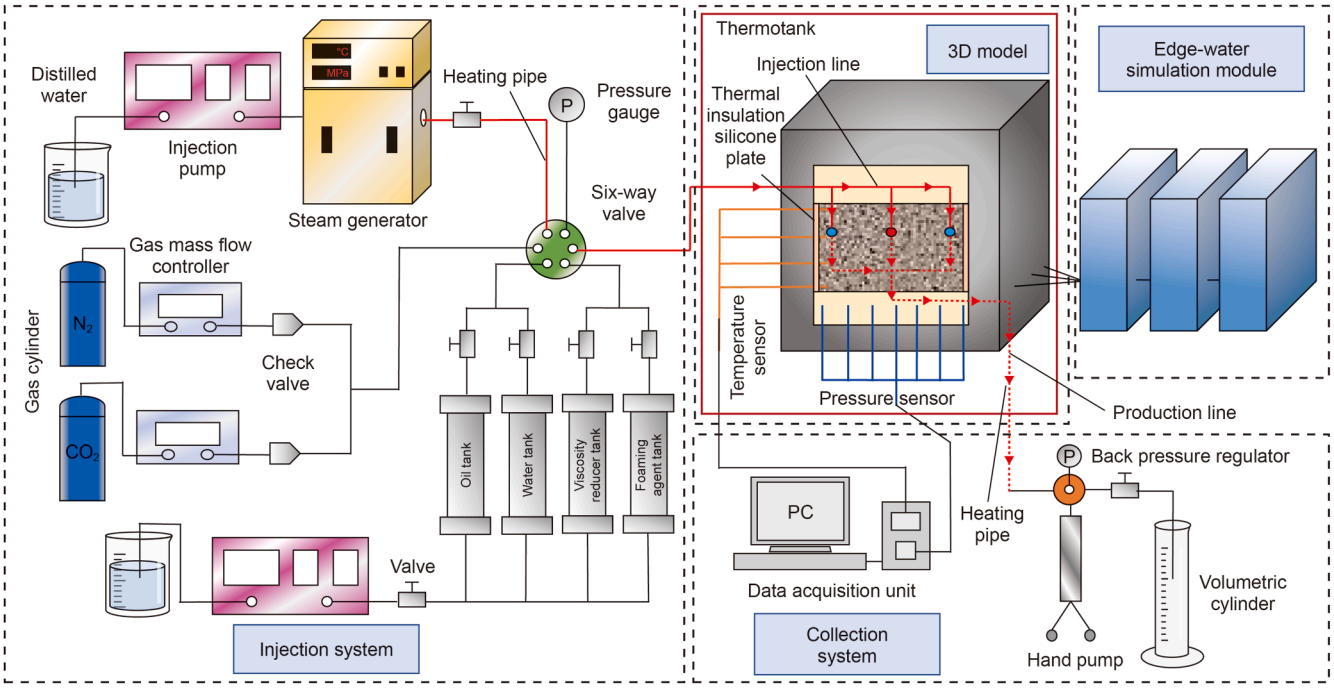

Fig. 3. Schematic of 3D physical simulation apparatus.

viscosity–temperature curve (illustrated in Fig. 5) was measured under an atmospheric pressure condition using degassed oil sample. It revealed strong thermal sensitivity of this oil sample, which suggested its high suitability for thermal recovery.

Model filling materials: The model was packed with 20–40 mesh and 60–80 mesh quartz sands to simulated reservoir heterogeneity, as these sands exhibited similarity thermal and physical properties to reservoir rock. Impermeable clay was used to simulate the top and bottom layers, separated from the oil layer by a tetrafluoro plate (inert and heat-resistant material stable up to 350 °C) to prevent clay–oil interactions that could affect displacement efficiency. The inner model walls were lined with thermally insulating silicone plate to reduce heat loss. The edge-water module used formation water doped with a fluorescent agent that emitted blue light under ultraviolet illumination, allowing visualization of edge-water invasion. The experimental oil and formation water were sourced directly from the field. Relevant materials are shown in Fig. 6.

Injection component materials: The injection components included industrial-grade nitrogen and carbon dioxide (purity: 99.99%), water–soluble VR (0.5 wt%), and foaming agent (0.6 wt%). Both VR and foaming agent were sourced from a heavy oil field in China, where their typical field concentrations were 0.3 and 0.5 wt%, respectively. To compensate for thermal degradation and adsorption during displacement, the VR concentration was increased to 0.5 wt%. The foaming agent concentration was set slightly above its critical micelle concentration (0.5 wt%) to ensure effective foam generation. To ensure sufficient fluorescence intensity under ultraviolet irradiation, the fluorescent agent concentration was selected as 2 wt%. Distilled water was used for superheated steam production to prevent scaling in the injection pipeline.

3.4. Conversion of similarity criterion

In the 3D physical simulation, parameter conversion based on similarity criteria is essential. The criteria used are listed in Table 1. In this study, key parameters including oil/water properties, reservoir pressure/temperature, and the thermal characteristics of quartz sand, were consistent with field conditions. Fundamental parameters for model construction and experimental procedures were derived accordingly. This approach effectively translated field conditions to laboratory scale. Prior to conversion, an appropriate scaling ratio $r(L)$ must be established, typically defined as follows:

$$r(L) = \frac{H_e}{H_r} = \frac{L_e}{L_r} \tag{2}$$

where subscripts e and r represent experimental model and oil field respectively.

Experimental well spacing: The net pay in the oil field is 48 m. For the experimental model, this dimension was scaled down to 18 cm, resulting in a scaling ratio $r(L) = (18\text{ cm})/(48\text{ m}) = 0.00375$. Given an actual well spacing of 100 m, the corresponding scaled well spacing in the model was calculated as 37.5 cm. In our experiments, this value was set to 38 cm to exactly match the size of the 3D model when simulating the well placement.

Experimental well length: The practical well length is 450 m, accordingly, the model well length should be 169 cm. However, due to the limitation of the model, the largest simulated well length was only 42 cm, which indicated we only simulated nearly one fourth of the actual well length.

Experimental permeability: According to the similarity criterion number π_1, it can be obtained that:

$$\left(\frac{K\rho_o g t}{\phi \Delta S \mu_o L}\right)_r = \left(\frac{K\rho_o g t}{\phi \Delta S \mu_o L}\right)_e \tag{3}$$

$$Re = \frac{K\rho_f^2 L_1 g}{\mu_f^2} \tag{4}$$

Given a field permeability of 0.5–2.0 μm^2, the model permeability should be scaled to 100–400 μm^2. However, to ensure fluid flow in the porous medium adhered to Darcy's law and maintained

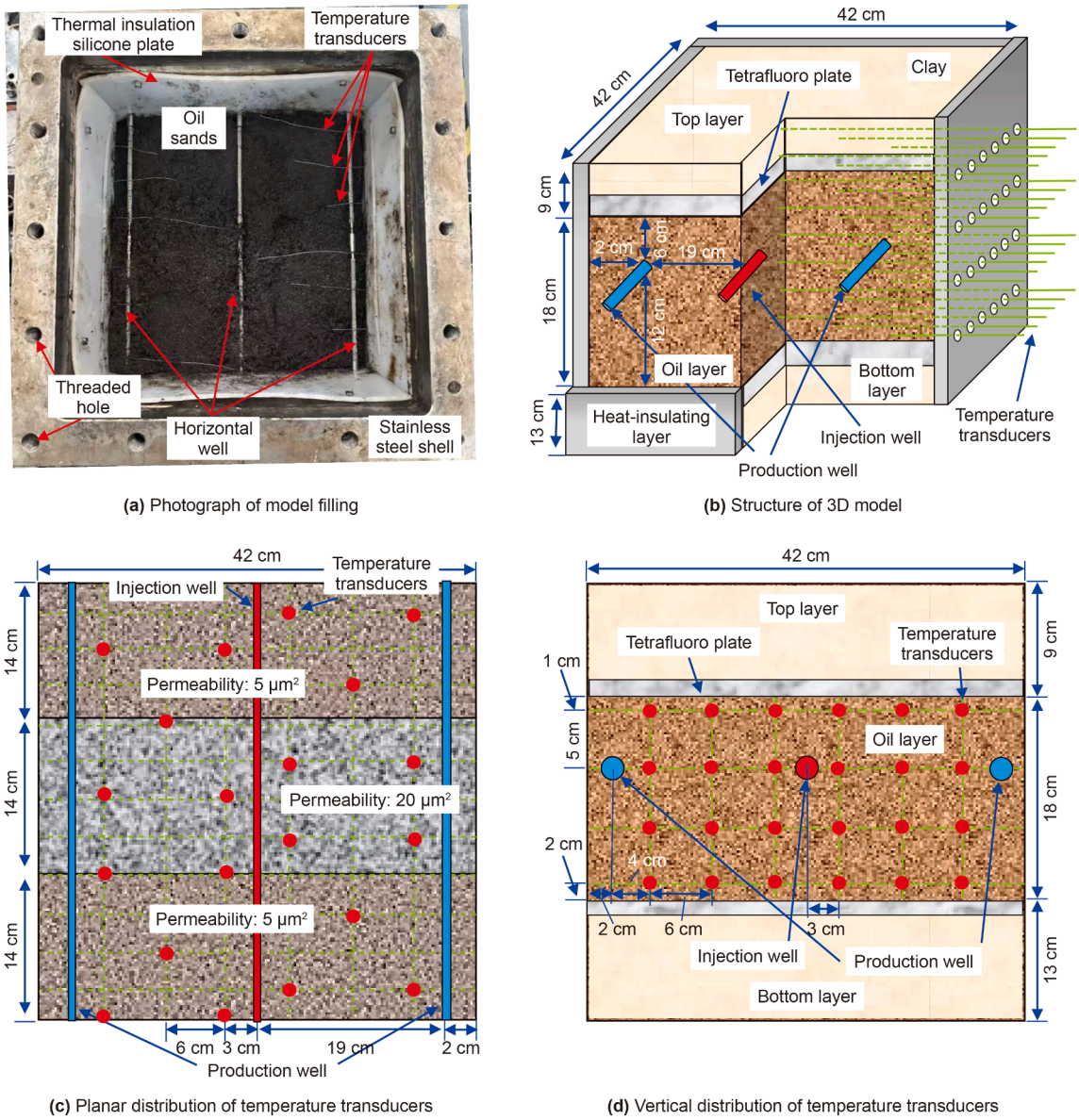

(a) Photograph of model filling

(b) Structure of 3D model

(c) Planar distribution of temperature transducers

(d) Vertical distribution of temperature transducers

Fig. 4. Schematic of the 3D model and temperature-measuring-point distribution.

Table 2
Characteristics of oil sample and formation water.

Oil density, g/cm^3	Oil viscosity @ 54 °C, mPa·s	Content of colloid and asphaltene in oil, %	Freezing point of oil, °C	Type of formation water	Formation water salinity, mg/L
0.96	2908	33.58	8	$CaCl_2$	18453

kinetic similarity, Reynolds number was used as a constraint (Eq. (4)). According to Forchheimer's law, when the Reynolds number exceeds 10, flow deviates from Darcy's law in high-permeability media (Dong et al., 2022b). Based on this principle, if we applied the following parameters, $\rho_f = 1000$ kg/m^3, $L_1 = 0.42$ m, $g = 10$ m/s^2, $\mu_f = 4$ mPa·s, It can be calculated that the permeability cannot be greater than 38 μm^2. Therefore, we set the permeability of the high and low permeability zones to about 20 and 5 μm^2, respectively, when filling the model.

Experimental gas injection volume and time: From the criterion π_2, we can obtain that:

$$\left(\frac{i_s t}{\phi \Delta S \rho_f L^3}\right)_r = \left(\frac{i_s t}{\phi \Delta S \rho_f L^3}\right)_e \quad (5)$$

In the field SF process, the injection volume of steam is 300 m^3/d per well, total 109,500 m^3 annually. Since we only simulate one-fourth of the well section, according to Eq. (5), we can calculate that the total injection volume of steam in the laboratory should be 1443.6 cm^3.

Regarding time conversion, although the permeability of different quartz sand was pre-calibrated via water injection

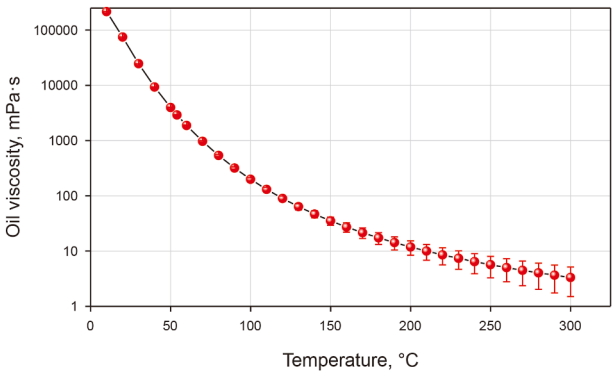

Fig. 5. Viscosity–temperature curve of the target oil sample.

permeability method, the overall permeability of the 3D model was not measured after packing. Consequently, model permeability was estimated based on individual sand properties, and the accuracy of time calculation using Eq. (3) could not be fully ensured. So, we scaled the annual field steam injection volume to the laboratory and combined with the injection pump rate (40 mL/min) to calculate that one year of field operation corresponded to 36.09 min in the laboratory.

Experimental chemical agent dosage: In the process of MCCSF, NCG and chemical agent were co-injected simultaneously. By specifying injection volume (0.2 PV) and injection rate (80 mL/min) of NCG, the injection time of NCG and chemical agent for each stage was calculated as about 24 min. Then the corresponding total cold-water equivalent of steam injection during this time was 960 mL. Combined with the concentration of each chemical agent, it can be obtained that 4.8 and 5.8 mL of VR and foaming agent were injected in each stage respectively.

Based on the similarity criteria conversion, detailed experimental parameters were obtained as shown in Table 3. Some parameters were appropriately adjusted for practicality. For instance, the well radius at field scale is about 0.1 m. If the well radius of experimental scale is converted strictly according to the similarity criterion, the result is only 0.0375 cm, which is a very small value. On the one hand, such a small well radius leads to excessive capillary force, and the fluid flow is somewhat similarly to seepage rather than pipe flow in experiment, which cannot guarantee the similarity in fluid dynamics. On the other hand, this scale is too difficult to process experimental tools. Therefore, we have enlarged the well radius to 0.6 cm. Steam injection rate was also modified considering the limitation of laboratory pump speed and pump capacity. At the same time, the well length was also limited by the experimental conditions, and only one fourth of the actual well length was simulated. As noted, relaxing certain parameters is necessary to satisfy geometric, kinetic, and dynamic similarity, ensuring successful experimental implementation.

3.5. Design results of edge-water module

In this experiment, three layers of external water aquifers were established: two oil sand-pack aquifers and one water sand-pack aquifer. The water sand-pack aquifer was positioned at the bottom of the model, while the two oil sand-pack aquifers were located 9 and 18 cm above it, respectively. Based on the parameters in Table 4, the calculated water and gas tank volumes for each aquifer were 2.70414 L (water) and 0.90138 L (gas) for the first oil sand-pack aquifer, 2.70416 L (water) and 0.90139 L (gas) for the second oil sand-pack aquifer, and 2.70418 L (water) and 0.90139 L (gas) for the water sand-pack aquifer. Given the negligible differences between these calculated volumes, uniform tank volumes of 2.7 L for water and 0.9 L for gas were implemented for all three aquifer layers.

3.6. Experimental procedures

Experimental preparation: The permeability of quartz sands with different mesh sizes was determined through water injection permeability method, the test results are shown in Fig. 7. Sands were cleaned to remove fine particles that could block production wells or affect accuracy. The oil sample was degassed and dehydrated, and its physical and chemical properties—including density, viscosity, and composition—were measured. Additionally, materials such as clay, tetrafluoro plates, heat-resistant gel, graphite strips, and distilled water were prepared in adequate quantities. Prior to model filling, temperature and pressure sensors were calibrated to ensure measurement reliability.

3D model filling: First, fluorescent agent solution and oil were mixed with quartz sands to prepare water and oil sands. Clay and tetrafluoro plates were then used to construct the top and bottom layers ((Fig. 8(a–d)), with the oil layer in between (Fig. 8(b)). Simulated wells, wrapped in wire mesh to prevent sand blockage, were placed in designated positions along with temperature sensors (Fig. 8(c)). The model was then sealed with graphite strips and heat-resistant gel, and connected to the edge-water simulation module.

Seal testing: After the model assembled, high-pressure nitrogen gas was injected into model until the pressure reached 12.0 MPa. The high-pressure environment was then maintained for 12 h to ensure good airtightness of the model.

(a) Fluorescence reaction (fluorescent solution vs. distilled water)

(b) Clay filling for top/bottom layers

(c) Tetrafluoro plate

(d) Thermal insulation silicone plate

Fig. 6. Some of the materials used in the experiments.

Table 3
The parameters of field scale and experiment scale.

Category		Parameter	Field	Experiment
Basic properties		Well pattern	Horizontal well	Horizontal well
		Well radius	0.1 m	0.6 cm
		Well spacing	100 m	38 cm
		Well length	450 m	42 cm (1/4 of total length)
		Net pay	48 m	18 cm
		Porosity	30%	30%
		Initial oil saturation	70%	70%
		Absolute permeability	0.5–2.0 μm^2	5–20 μm^2
		Permeability ratio	4	4
		Viscosity of degassed oil at 54 °C	2908 mPa·s	2908 mPa·s
		Initial temperature	54 °C	54 °C
		Initial pressure	12.0 MPa	12.0 MPa
		Steam temperature	250 °C	250 °C
		Steam quality	0.7	0.7
		Reservoir dip	6°	6°
		Time	1 year	36.09 min
Injection–production parameters	SHP	Total steam injection volume per cycle	8000 m^3	105 cm^3
		Soak time	20 d	1.98 min
	PSF	Injection rate of steam	300 m^3/d	40 cm^3/min
	MCCSF	Injection rate of steam	300 m^3/d	40 cm^3/min
		Injection volume of NCG per stage	0.2 PV	0.2 PV
		Injection volume of VR per stage	–	4.8 cm^3
		Injection volume of foaming agent per stage	–	5.8 cm^3

Table 4
Conversion parameter table.

Parameter	Value
Internal oil–water boundary distance, m	200
External oil–water boundary distance, m	600
Length of sand-pack, m	1
Radius of sand-pack, m	0.02
Model length, cm	42
Reservoir thickness within the model, cm	18
Aquifer multiplier	10
Compressibility of formation water, MPa^{-1}	4.5×10^{-4}
Compressibility of oil sample, MPa^{-1}	2×10^{-3}
Similarity ratio	0.00375
Constraint coefficient	1
Pressure after displacement ceased, MPa	4

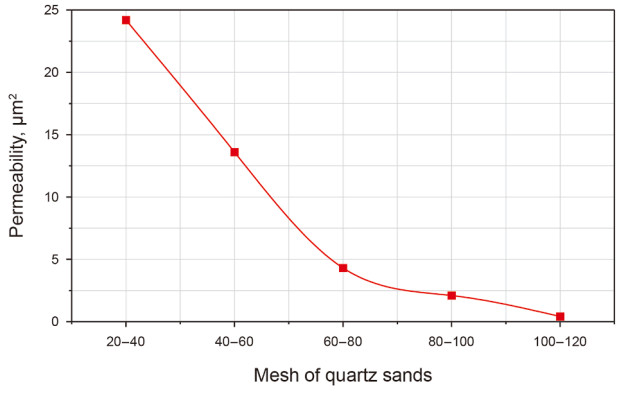

Fig. 7. Permeabilities of the quartz sands with different mesh.

Initial condition establishing: The model was placed in a thermotank and heated to the initial reservoir temperature. Preheating was considered complete when the temperature difference across sensors was within 2 °C. Oil was injected at 0.5 mL/min until pressures at all measurement points reached the target value.

Connection steps: After the oil sample and formation water were saturated in each layer of the sand-pack of the edge-water simulation module, the module was connected to the 3D model. During this process, the left valve of the multi-layer sand-pack were kept closed. Then, the 3D model and edge-water simulation module were separately pressurized to reservoir pressure to ensure that the oil–water distribution in the 3D model was not disturbed. During pressurization, the right valve of the multi-layer sand-pack was opened, and volumes of water and gas tanks in each layer were set according to the calculation results. Formation water and nitrogen were then injected, while nitrogen was continuously injected through the gas cylinder to raise the pressure. When the readings of pressure gauges 1 and 2 in each layer stabilized and reached the target reservoir pressure, the gas cylinder was closed and the left valve of the sand-pack were opened to complete the connection with the 3D model.

Steam debugging: Before injecting steam into the model, the steam generator was preheated to ensure that key parameters, such as flow rate, temperature, and steam quality, met the specified requirements.

Setting up backpressure: A back-pressure valve was used to control outlet pressure. To maintain steam in the gas phase during thermal recovery, outlet pressure is typically set 0.5 MPa below the steam saturation pressure (Hong et al., 2025). At 250 °C, the steam saturation pressure is about 4 MPa, so the valve was set to about 3.5 MPa at SF stage. Additionally, the outlet line was wrapped with a constant-temperature heating belt at 80 °C to prevent cold oil from clogging the production line.

Steam huff and puff: Before initiating SF, eight cycles of SHP were conducted to preheat the reservoir. During this process, three wells were simultaneously injected and produced, each cycle was terminated until no liquid being produced.

Steam flooding: After SHP, two SF experiments were conducted for comparison: Exp. A (PSF) with steam injection only, and Exp. B (MCCSF) involving multi-component injection at different stages. In both cases, the intermediate well was used for injection, the side wells for production. In the process of MCCSF, the components of each stage, including steam, NCG, and chemical agent, were injected simultaneously. The experiment ended when the

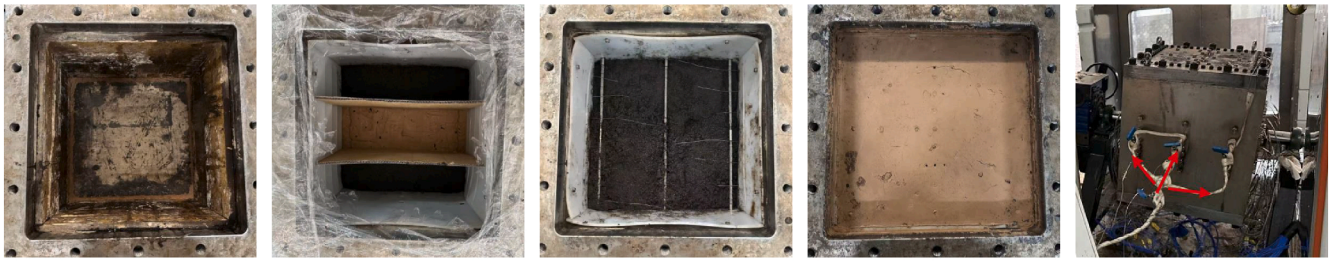

Fig. 8. The 3D model preparation process.

instantaneous oil–steam ratio dropped below 0.1. Temperature and pressure fields were monitored in real time, while oil and water production rates were continuously recorded to identify flooding stages and calculate the oil–gas ratio. The oil recovery factor was then determined based on the experimental data.

4. Experimental analysis method

4.1. Method for determining remaining oil saturation

In 3D physical experiments, remaining oil saturation is commonly measured via kerosene extraction, a method limited by high workload, complex procedures, low accuracy, and susceptibility to human error. In previous work, we developed a grayscale analysis algorithm that correlated grayscale values with oil saturation for regional quantification of remaining oil (Hong et al., 2025). In this study, the approach was further refined by establishing a grayscale–temperature–oil saturation relationship to validate grayscale labeling, allowing quantitative analysis across all layers and regions. The flowchart of this method is shown in Fig. 9. Since real-time observation of oil sand color changes is not feasible during 3D experiments, representative samples were selected from distinct thermal regions—steam chamber (SC), thermal front (TF), hot water zone (HWZ), and low temperature zone (LTZ)—with paired samples from high and low permeability (HP/LP) regions. Oil saturation in these subsamples was measured via kerosene extraction. Additionally, images of saturated oil sands (SOS) and clean oil sands (COS), along with corresponding measurements, were used to validate the accuracy of grayscale labels.

The calculated mean square errors between measured and predicted oil saturations were 1.03 for Exp. A and 1.06 for Exp. B, with correlation coefficients of 0.9983 and 0.9984, respectively. The absolute error boxplots (as shown in Fig. 10) showed low prediction errors with no outliers, confirming the stability and accuracy of the grayscale algorithm. Finally, grayscale values in the selected area were mapped to the corresponding oil saturation based on grayscale labels (illustrated in Table 5) and the average oil saturation was calculated through weighted computations by algorithm recognition module.

$$S_{oa} = \frac{\sum_{i=1}^{n} S_{oi}}{u} \tag{6}$$

4.2. Identification method of water invasion theory

In previous work, we analyzed the heat absorption of rocks saturated with oil and water, finding that water-saturated rocks had significantly higher heat capacity. Thus, during thermal recovery, the slope of the temperature–time curve decreased noticeably after water invasion (Pang et al., 2021). Based the

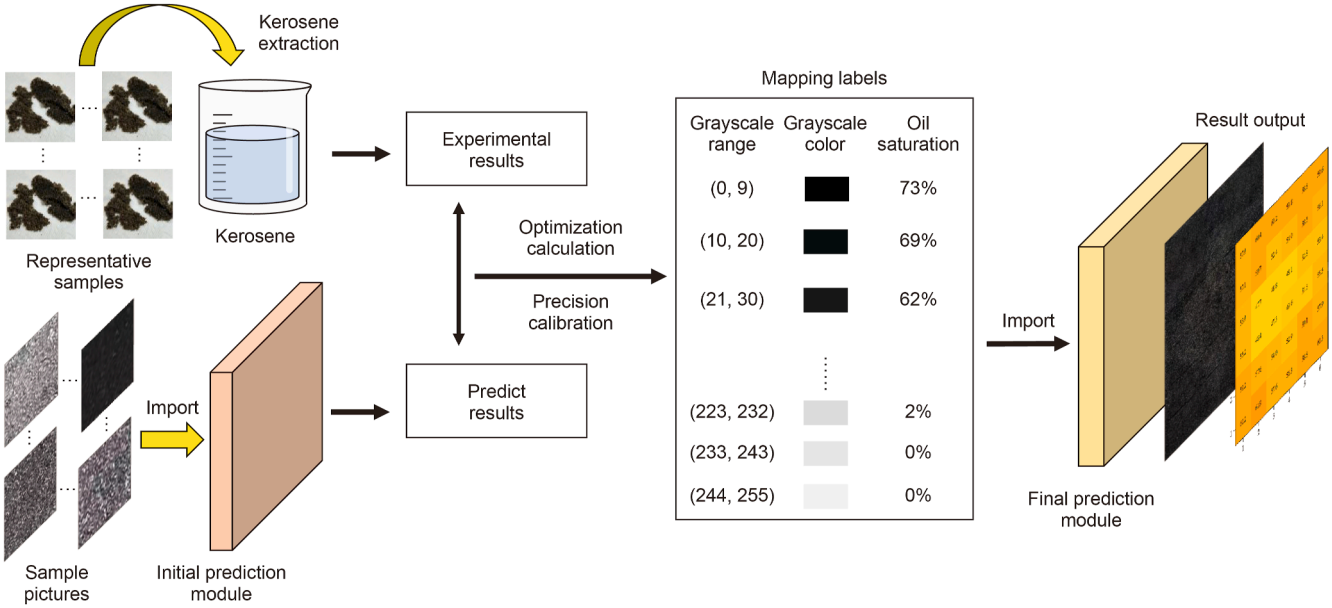

Fig. 9. Flow chart of establishing quantitative analysis method of remaining oil saturation.

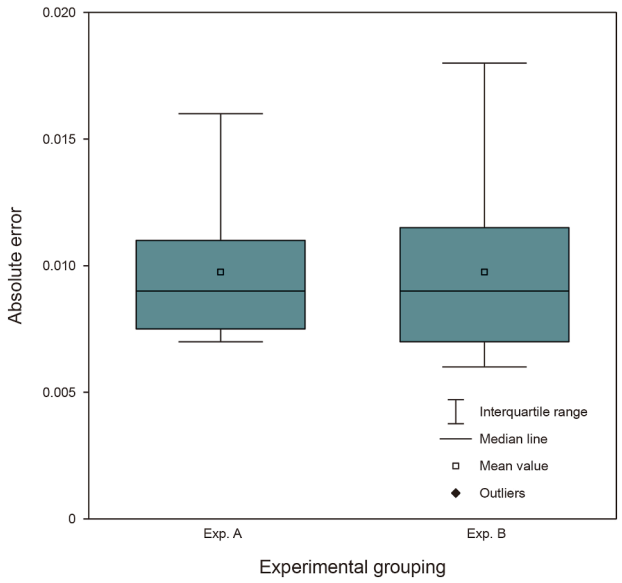

Fig. 10. Absolute error box plot of validation results.

recorded thermocouple data in the displacement process, we theoretically determined the basic range of water invasion and used it to assist in verifying the experimental design of multiple external water aquifers.

$$\frac{\partial T}{\partial t}=\frac{1}{M_{\mathrm{ro}}}\left(B\nabla^2 T-\nu_{\mathrm{t}}M_{\mathrm{o}}\nabla T\right)\propto\frac{1}{M_{\mathrm{ro}}} \tag{7}$$

$$\frac{\partial T}{\partial t}=\frac{1}{M_{\mathrm{rw}}}\left(B\nabla^2 T-\nu_{\mathrm{t}}M_{\mathrm{w}}\nabla T\right)\propto\frac{1}{M_{\mathrm{rw}}} \tag{8}$$

5. Experimental results and analysis

5.1. Production performance

Prior to SF, both Exps. A and B underwent eight cycles of SHP to replicate field production conditions, achieving reservoir preheating and pressure reduction. After eight cycles, reservoir pressure decreased from 12 MPa to approximately 4 MPa. The cumulative oil recovery factors were 14.62% for Exp. A and 13.87% for Exp. B. As shown in Fig. 11, the overall production performance curves of SHP exhibited similar trends, indicating that this type of experiment has certain repeatability and providing a reliable basis for comparison between the two experiments.

In the early stage of SF, Exp. B employed a composite steam formulation containing CO_2 and VR, which accelerated thermal connection between injection and production wells and led to a faster increase in oil production. As a result, Exp. B entered the high production phase at about 30 min after SF initiation, which was approximately 20 min earlier than Exp. A. Subsequently, nitrogen foam was injected twice in Exp. B (at 50 and 250 min) to pre-adjust the reservoir profile and mitigate channeling. These foam treatments led to significant improvements in production performance. At stable displacement stage, the peak oil production rate and oil–steam ratio reached 16.6 mL/min and 0.414, respectively, which were 4 mL/min and 0.053 higher than Exp. A. Moreover, the duration of the stable high-production period in Exp. B extended to approximately 0.7 PV (166.7 min), which was about 0.3 PV (71.4 min) longer than that of Exp. A. During the thermal connection and stable displacement phases, both experiments maintained low water cut levels. Due to the water suppression effect of foam (Wei et al., 2024; Soomro, 2025) in the multi-component system, Exp. B exhibited an average water cut 5%–10% lower than Exp. A. Without auxiliary measures, Exp. A experienced channeling at about 190 min, leading to a sharp increase in water cut and a decline in both oil–steam ratio and oil production. In contrast, Exp. B delayed channeling to 220 min through pre-channeling profile adjustment and post-channeling plugging, with softer slope in water cut. As displacement progressed, both experiments entered the thermal erosion stage, characterized by low instantaneous oil production and oil–steam ratio, with water cut levels exceeding about 95%. Exp. A was terminated when the oil–steam ratio dropped below 0.1 after flooding 3.80 PV, achieving a final oil recovery of 43.66%. In Exp. B, when the instantaneous oil–steam ratio dropped to around 0.15, an EOR method was implemented that was using CO_2 and VR co-injected with steam. This briefly boosted oil production to 4.78 mL/min and the oil–steam ratio to 0.193, while reducing the

Table 5
Grayscale-oil saturation mapping labels and verification results of Exps. A and B.

Grayscale range	Grayscale color	Grayscale range	Grayscale color	Experimental image (Exp. A)				Corresponding oil saturation (Exp. A), %		Experimental image (Exp. B)				Corresponding oil saturation (Exp. B), %	
				Location	Picture	Laboratory measured saturation, %	Algorithm calculated saturation, %			Location	Picture	Laboratory measured saturation, %	Algorithm calculated saturation, %		
(0, 9)		(127, 137)		SC-HP		15.3	15.8	75.0	16.0	SC-HP		7.0	7.9	73.0	15.0
(10, 20)		(138, 147)		SC-LP		18.2	19.3	70.0	14.0	SC-LP		8.2	9.2	69.0	10.0
(21, 30)		(148, 158)		TF-HP		22.1	23.7	65.0	12.0	TF-HP		15.2	16.5	62.0	9.0
(31, 41)		(159, 169)		TF-LP		25.7	24.8	60.0	10.0	TF-LP		17.1	18.9	57.0	8.0
(42, 52)		(170, 179)		HWZ-HP		33.9	33.4	55.0	9.0	HWZ-HP		23.5	24.3	55.0	7.0
(53, 62)		(180, 190)		HWZ-LP		36.7	36.9	50.0	8.0	HWZ-LP		26.8	25.7	50.0	6.0
(63, 73)		(191, 200)		LTZ-HP		60.1	58.5	45.0	7.0	LTZ-HP		56.1	55.4	43.0	5.0
(74, 84)		(201, 211)		LTZ-LP		63.3	62.2	40.0	6.0	LTZ-LP		61.6	60.9	38.0	4.0
(85, 94)		(212, 222)		SOS-HP		70.9	69.7	35.0	5.0	SOS-HP		69.2	69.8	36.0	3.0
(95, 105)		(223, 232)		SOS-LP		72.3	71.9	30.0	4.0	SOS-LP		70.5	69.3	30.0	2.0
(106, 115)		(233, 243)		COS-HP		0	0.9	25.0	2.0	COS-HP		0	0.7	25.0	0
(116, 126)		(244, 255)		COS-LP		0	1.1	20.0	0	COS-LP		0	0.9	20.0	0

Notes: In Exp. A, grayscale values in the range (0, 126) correspond to oil saturations of 75% to 20%, while values in (127, 255) correspond to saturations of 16% to 0. In Exp. B, the same grayscale intervals (0, 126) and (127, 255) correspond to oil saturations of 73% to 20% and 15% to 0, respectively.

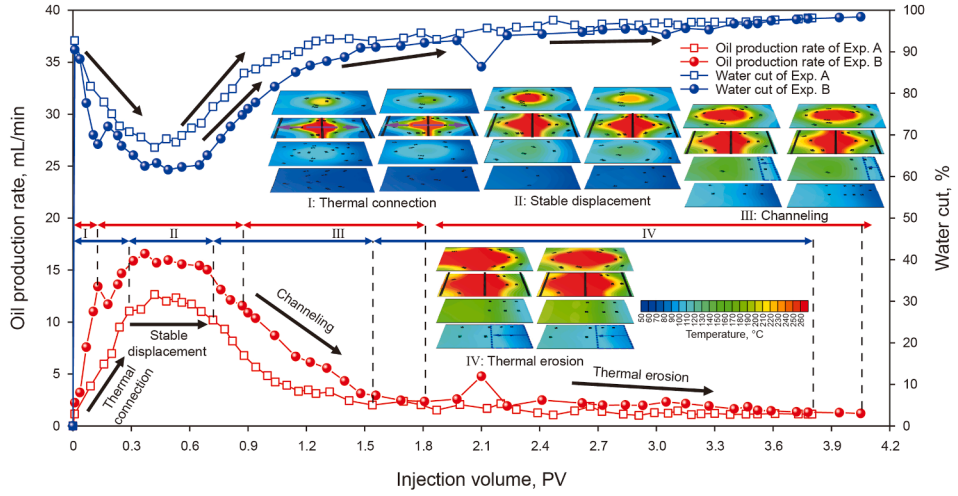

(a) Oil production rate and water cut curves of Exps. A and B

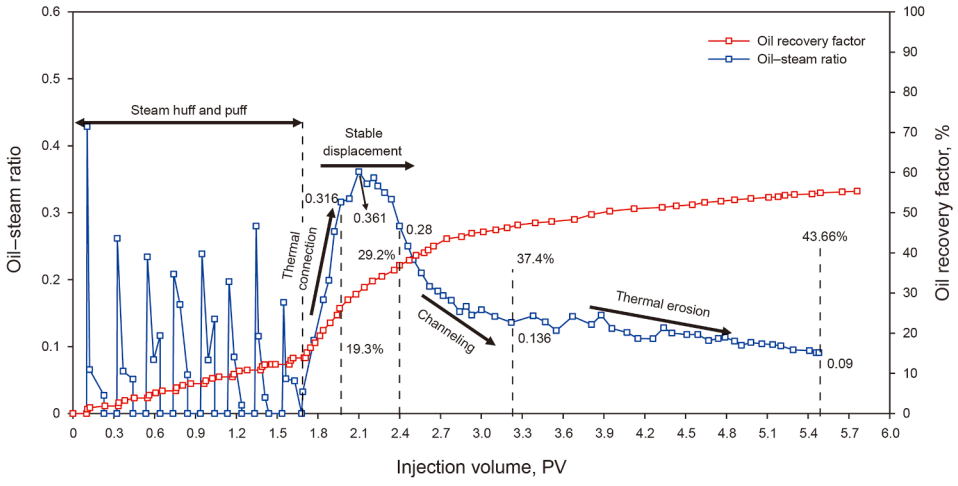

(b) Oil–steam ratio and oil recovery factor curves of Exp. A

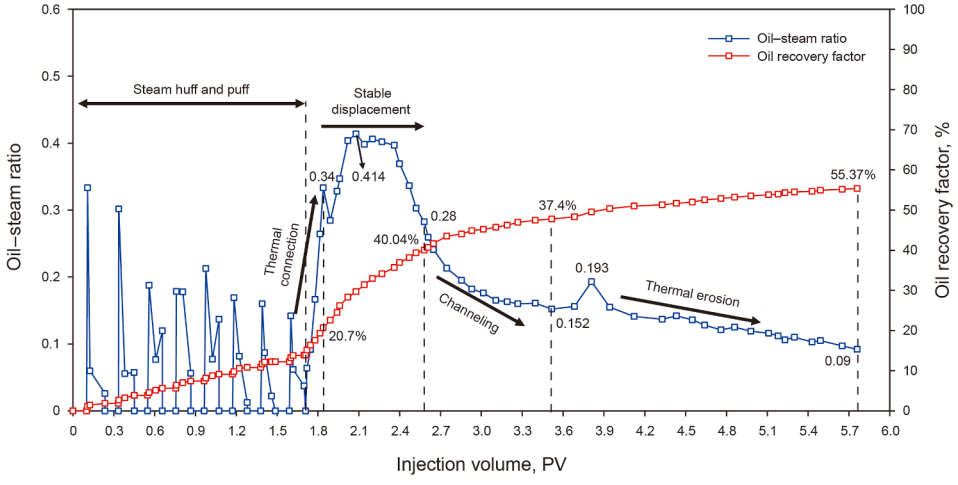

(c) Oil–steam ratio and oil recovery factor curves of Exp. B

Fig. 11. Production performance curves of Exps. A and B.

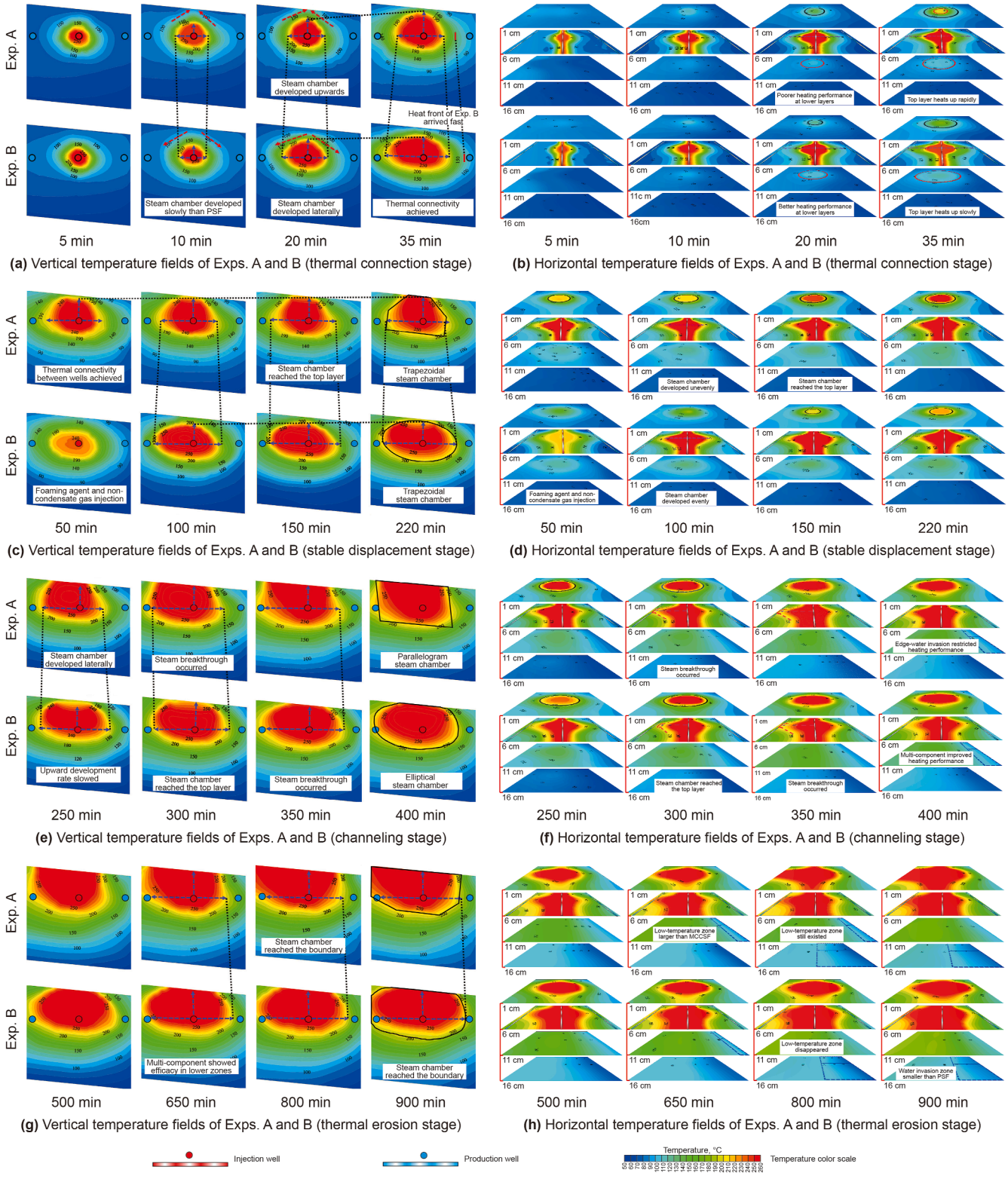

(a) Vertical temperature fields of Exps. A and B (thermal connection stage)

(b) Horizontal temperature fields of Exps. A and B (thermal connection stage)

(c) Vertical temperature fields of Exps. A and B (stable displacement stage)

(d) Horizontal temperature fields of Exps. A and B (stable displacement stage)

(e) Vertical temperature fields of Exps. A and B (channeling stage)

(f) Horizontal temperature fields of Exps. A and B (channeling stage)

(g) Vertical temperature fields of Exps. A and B (thermal erosion stage)

(h) Horizontal temperature fields of Exps. A and B (thermal erosion stage)

Fig. 12. Comparison of vertical and horizontal temperature field evolution during the flooding stage in Exps. A and B.

water cut from 92% to 86%. This EOR phase lased about 0.2 PV (47.6 min) and Exp. B ultimately reached the point of 0.1 oil–steam ratio after flooding 4.05 PV, extending displacement by 0.25 PV (59.5 min) compared to Exp. A, and achieving a final oil recovery of 55.37%.

5.2. Steam chamber expansion characteristics

By interpolating the collected thermocouple data, the vertical and horizontal development of the temperature fields at different displacement stages was obtained, as shown in Fig. 12.

5.2.1. Thermal connection

In the initial stage of thermal connection, the steam chamber in Exp. B developed slightly more slowly than in Exp. A due to the injection of low-temperature CO_2 and VR. Vertical and horizontal temperature profiles revealed that, with progression, injected steam in both experiments tended to accumulate at the reservoir top due to dip angle and gravity segregation. As a result, the steam chamber in Exp. A developed predominantly upward. In Exp. B, however, CO_2 rapidly formed a gas cap at the top, exerting downward pressure that promoted lateral steam chamber expansion. Due to the low thermal conductivity of CO_2, the top reservoir temperature in Exp. B remained 25 °C lower than in Exp. A, effectively reducing heat loss and improving steam thermal efficiency. VR showed strong effect within the well layer. By enhancing thermochemical viscosity reduction (Li et al., 2011), it accelerated temperature development and improved thermal connectivity between injection and production wells. Coupled with the auxiliary viscosity reduction effect of CO_2, the movable oil front and the thermal front developed rapidly, especially in lower production wells. At 30 min after the start of SF, the thermal front in Exp. B had already approached the production wells, whereas Exp. A required nearly 50 min. Moreover, Exp. A exhibited poor thermal response in lower wells, with a maximum temperature difference of nearly 45 °C between upper and lower wells, compared to approximately 20 °C in Exp. B. This indicated that CO_2 and VR mitigated the uneven steam chamber growth caused by steam override and reservoir heterogeneity, while also shortening the thermal connection time.

In the lower reservoir layers, due to the pressure maintenance and oil displacement effects of the CO_2 cap and VR, the heated zone in Exp. B was more uniform, approximating a circular shape. In comparison, Exp. A displayed a narrower heated zone concentrated directly below the injection well, with a noticeably smaller circular area. On average, the lower reservoir in Exp. B was 10 °C warmer than in Exp. A due to reduced heat loss and more uniform heating. In the bottom reservoir layer, the temperature fields between the two experiments showed little difference. Heating was difficult to achieve effectively during the thermal connection stage in this zone because of the influence of edge-water invasion and spatial positioning.

5.2.2. Stable displacement

At the onset of the stable displacement stage, Exp. B adopted a nitrogen foam profile control strategy to adjust steam suction profile and delay channeling, resulting in a slight temperature decline in the steam chamber. In contrast, Exp. A, lacking such measures, continued to exhibit predominantly vertical steam chamber growth. Particularly within the well layer, where steam preferentially channeled through high-permeability paths to the upper well caused severe steam override. By 150 min after SF began, steam chamber in Exp. A had reached the reservoir top, leading to significant performance disparities between upper and lower production wells, which was nearly 40 °C. In Exp. B, the NCG cap maintained the top reservoir temperature 25 °C lower than in Exp. A, delaying steam breakthrough at the top and enhancing thermal efficiency. Following foam-based profile control, the NCG foams increased the flow resistance in high-permeability zone by Jamin effect that forced some of injected steam flow to low-permeability zone (Lyu et al., 2018). This made steam displacement more uniform and lead to lateral chamber expanding. Although upward growth remained dominant within the well layer, the temperature differential between upper and lower wells was reduced to 20 °C, and the high-temperature zone area was larger than in Exp. A. The multi-component system significantly improved displacement efficiency and sweep efficiency.

In the lower reservoir, temperature differences between experiments remained modest, with Exp. B generally 10 °C warmer than Exp. A. The heated zone in Exp. B expanded outward in a circular pattern, whereas in Exp. A it remained concentrated around the injection well. Due to the dip angle and high-permeability channels, both experiments exhibited upward development of the heated zones, with typical vertical temperature differences around 20 °C which suggested that the multi-component system had limited influence in this region. Heating in the bottom layer remained minimal in both cases, though the temperature field showed a downward expansion trend. Continuous analysis of the vertical temperature field revealed that the lateral sweep area in Exp. B was significantly larger than in Exp. A, indicating more uniform displacement. In this stage, the steam chamber in Exp. B exhibited an elliptical morphology with lower inter-well thermal variation, while Exp. A formed a trapezoidal chamber exhibiting greater thermal response heterogeneity.

5.2.3. Channeling

At the beginning of this stage, nitrogen foam was injected in Exp. B for profile control. As the steam chamber was already well developed, its overall temperature remained relatively stable. In Exp. A, once the steam chamber reached the top reservoir, it began to expand laterally in the upper section. The lateral expansion of the temperature field in the middle–upper layers accelerated, and the steam chamber shape transitioned from trapezoidal to parallelogram. Although heat transfer to lower zones slightly improved, significant vertical disparities persisted, with steam breakthrough at the upper production well occurring around 300 min. In Exp. B, the cumulative effect of two profile control treatments reduced the development rate near high-permeability zones, diverting steam toward lower-permeability and deeper regions. As a result, the steam chamber reached the reservoir top 150 min later than in Exp. A and maintained an elliptical shape. Steam breakthrough at the upper production well occurred at 350 min. By the end of this stage, temperatures near the upper production wells were similar in both experiments. However, the lower production well in Exp. B exhibited a stronger thermal response, with temperatures 15 °C higher than in Exp. A.

In the upper section of the lower reservoir, temperature differences narrowed with continued displacement, and both experiments showed a heat transfer trend from upper to lower zones. Nonetheless, the lower section of the lower reservoir in

Exp. B displayed significantly better thermal development, indicating effective suppression of edge-water invasion (as shown in blue box). In the bottom layer, differences remained minor. Although Exp. B showed slightly improved heating, overall thermal development was limited in both experiments. Heating in this zone relied primarily on conduction from upper layers, resulting in a 30 °C increase over initial reservoir temperature in both cases. However, due to reservoir depth and edge-water effects, displacement efficiency in this zone remained limited.

5.2.4. Thermal erosion

During this stage, Exp. B implemented assisted SF with VR and CO_2. In Exp. A, the steam chamber reached the upper reservoir boundary by 800 min, after which its expansion largely ceased. The final chamber resembled an inverted trapezoid, with significant displacement imbalance: the upper reservoir was nearly fully swept, while the lower region near the production well remained insufficiently displaced. The maximum temperature difference between upper and lower sections reached 100 °C. In contrast, the steam chamber in Exp. B reached the upper boundary near the end of the experiment. Due to the integrated effects of profile control, viscosity reduction, pressure maintenance, and composite flooding, steam chamber development was more extensive and uniform. The final chamber exhibited an elliptical shape with a larger cross-sectional area and a smaller temperature disparity between upper and lower sections of approximately 70 °C. The swept zone near the lower production well was notably larger than in Exp. A, indicating that the multicomponent system significantly improved displacement efficiency in the lower section.

Well-developed heating also led to more pronounced differences in the temperature fields of the lower and bottom layers. In Exp. B, temperature maps displayed more green tones and fewer blue zones, reflecting better thermal coverage. This also implied less extensive and less severe edge-water invasion (as shown in blue box). These findings further confirmed that MCCSF effectively mitigated the negative impact of edge-water and improved overall displacement performance.

5.3. Water invasion characteristic

Fluorescent water invasion was observed during sampling under ultraviolet illumination as shown in Fig. 13. In the PSF process of Exp. A, reservoir pressure remained relatively low (at approximately 3.7 MPa). The substantial pressure differential between reservoir and edge-water facilitated significant edge-water invasion, resulting in 48.8% water invaded area in the thermocouple-monitored fourth layer. Conversely, during the MCCSF process of Exp. B, the injection of NCG formed a gas cap that helped to sustain reservoir pressure. Additionally, foam generated from NCG and foaming agents enhanced the injection–production pressure differential while reducing the pressure difference between the reservoir and edge-water. Furthermore, NCG lowered steam partial pressure, allowing it to remain in the gaseous phase more readily at the same injection temperature, which also contributed to sustaining the reservoir pressure during displacement. Pressure monitoring showed that the reservoir pressure during flooding process was maintained at approximately 4.2 MPa, a 13.5% increase compared to Exp. A. The final water invasion area of Exp. B accounted for 34.7%.

Thermocouple data from the fourth monitored layer (as shown in Fig. 14) revealed water invasion characteristics through temperature-time curve slope analysis. Measurement points 2 and 3 experienced water invasion during the process of SHP, resulting in consistently low curve slopes. During the SF stage, edge-water preferentially channeled toward high permeability zones, with water breakthrough times at measurement points in high permeability zones generally earlier than those in low permeability zones. In the MCCSF process of Exp. B, edge-water invasion was significantly suppressed, with only 5 measurement points showing water invasion compared to 12 in Exp. A. The spatial correlation between invaded measurement points and the actual water invasion zones indirectly verified the

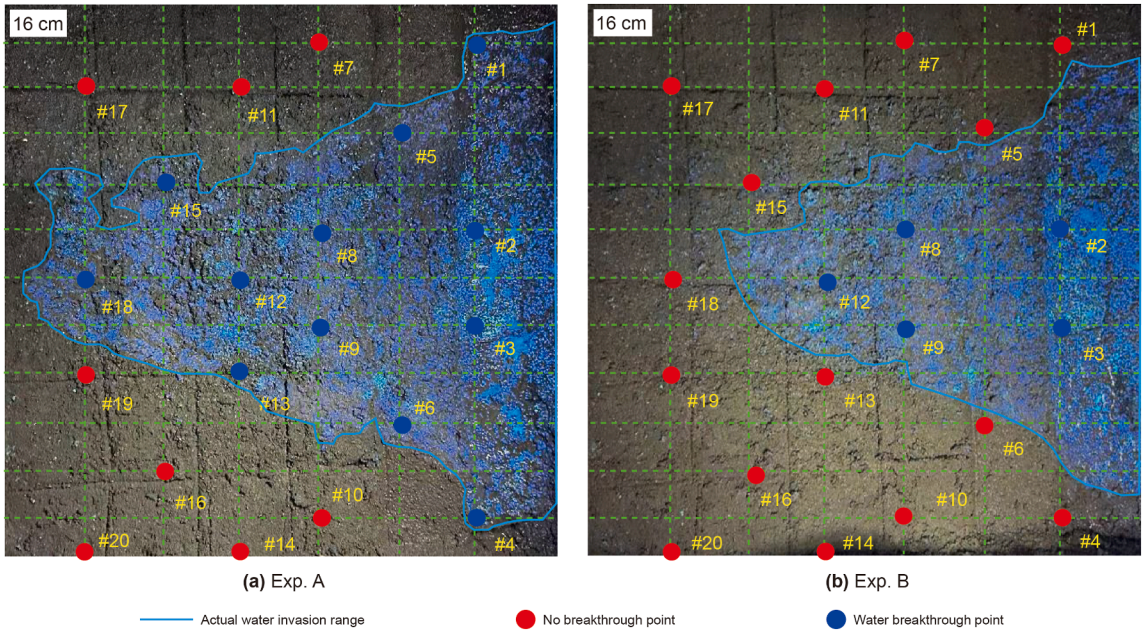

Fig. 13. Comparison of edge-water invasion in Exps. A and B.

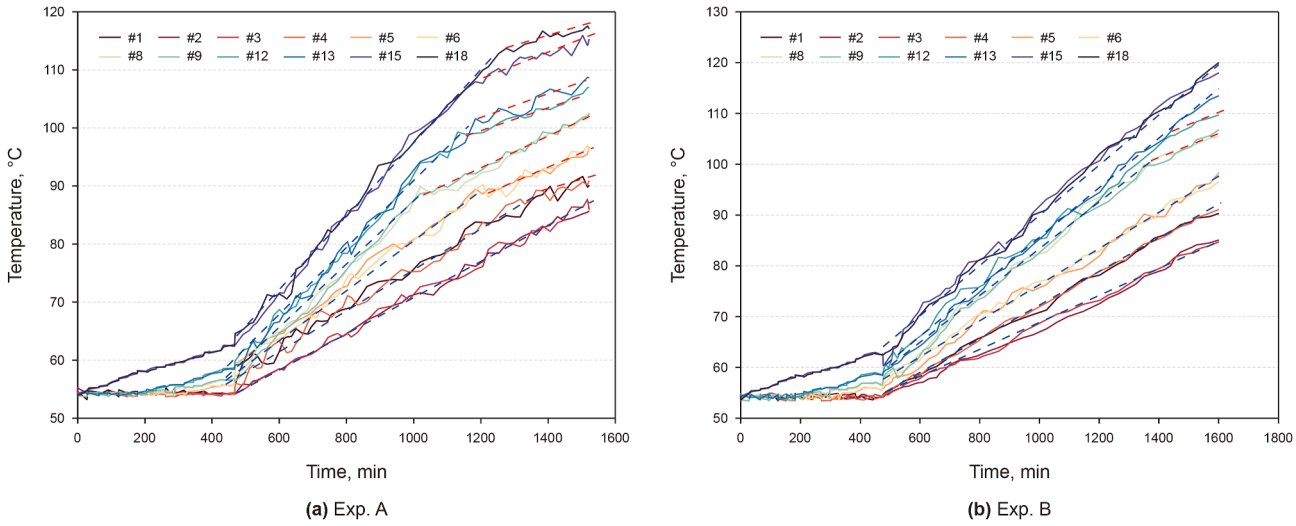

Fig. 14. Temperature–time curves of the fourth layer thermocouples in the experiments.

reliability of the multi-external aquifer simulation method for simulating edge-water.

5.4. Distribution of remaining oil

Fig. 15 shows the distribution of remaining oil in each layer for both experiments. To ensure consistency, all images were processed using OpenCV, including non-local means denoising, convergence enhancement and uniform brightness and contrast adjustment. Subsequently, a color thresholding method was then applied with identical threshold values for all images. In the processed images, lighter regions were rendered red, indicating high displacement efficiency and low oil saturation, while darker areas retained their original appearance, representing poorly swept zones with high oil saturation. Finally, combined with the results of the remaining oil heat map (as shown in Fig. 16) identified by the gray algorithm module, we can analyze the distribution of remaining oil and utilization degree of each layer at the end of displacement.

In the top reservoir layer, steam override caused heated crude oil to drain gravitationally toward flank production wells. This phenomenon resulted in pale-colored oil sands in both experiments, indicating efficient displacement. In Exp. A, steam preferentially channeled through high-permeability zones, with upper sections appearing significantly lighter than lower ones. However, dark residual oil remained in corner regions of both high and low sections, yielding an overall sweep efficiency of 90.6%. In contrast, Exp. B, employing MCCSF effectively mitigated steam override and achieved more uniform displacement. Only minor dark zones remained in the lower corners, with a sweep efficiency of 98.1%. The oil saturation heatmap in Exp. B showed predominantly green hues, indicating superior displacement across high/low permeability zones and corner regions. The average oil saturation in Exp. B was 13.06%, 9.35% lower than in Exp. A. Combined with temperature field analysis, the remaining oil saturation in the steam chamber, thermal front, and hot water zone of Exp. B averaged 8.59%, 14.92%, and 20.03%, respectively—compared to 16.73%, 19.63%, and 31.13% in Exp. A. These results demonstrated that the multi-component system enhanced overall displacement efficiency and improved oil recovery in corner zones.

In the well layer, after multiple cycles of SHF and subsequent SF, the oil sand appeared white in both experimental groups. However, Exp. A displayed slightly darker areas in the upper corner zones compared to Exp. B, which achieved comprehensive sweep efficiency in these regions. Due to reservoir dip and gas override, both experiments exhibited darker remaining oil zones in lower corner areas, but Exp. B had smaller and lighter zones than Exp. A. Sweep efficiencies were 91.3% for Exp. A and 95.9% for Exp. B. Color thresholded images revealed a distinct black oil zone around the central injection well, which attributed to high-temperature distillation of heavy oil causing deposition of heavy components (Dong et al., 2019). In Exp. B, the incorporation of VR, foaming agents, and CO_2 significantly mitigated the deposition of heavy components, thereby improving the steam sweep and displacement efficiency to some extent. Combined analysis of oil saturation heatmaps and temperature fields yielded average oil saturations of 21.22% for Exp. A and 11.91% for Exp. B in this layer. Average remaining oil saturations within the steam chamber, thermal front, and hot water zone were 18.09%, 23.69%, and 29.38% for Exp. A, respectively, compared to 9.20%, 13.88%, and 19.20% for Exp. B. These results demonstrated that MCCSF not only expanded the sweep area but also improved displacement efficiency across different thermal zones.

In the middle oil layer, both experiments exhibited a cross-shaped sweep pattern along the injection well and high-permeability zone. Influenced by formation dip and steam override, sweep progression favored the upper section in both cases, particularly in Exp. A where upper high-permeability zones were fully swept. However, significantly darker oil sands in lower high-permeability zones resulted in an overall areal sweep efficiency of 62.3%. Conversely, Exp. B demonstrated superior performance: injected non-condensable gas formed a gas cap while foam enhanced flow resistance, collectively maintaining stable pressure differentials during flooding. Combined with VR and foam-assisted sweep improvement, Exp. B achieved a larger, more uniform cross-shaped swept area with notably better lower-section coverage and lighter oil sand coloration, yielding 70.1% sweep efficiency. Oil saturation heatmaps revealed average saturations of 39.78% for Exp. A and 31.48% for Exp. B in this layer. Although the enhancement was less pronounced than in the upper reservoir, the multi-component system still significantly improved displacement effectiveness in the middle oil layer.

In the lower reservoir layer, displacement effectiveness was markedly inferior to middle and upper layers, evidenced by

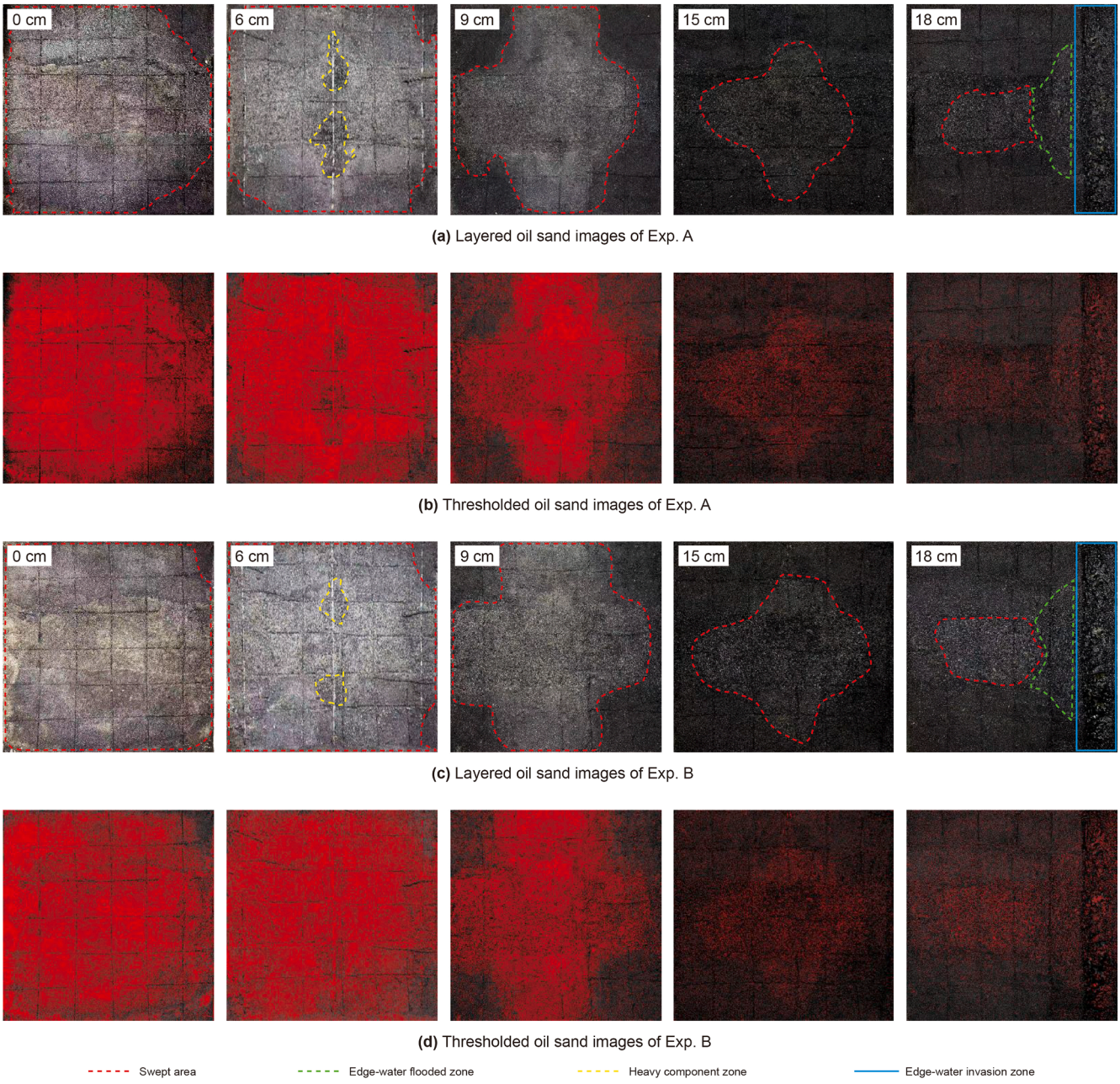

Fig. 15. Photos and thresholded images of oil sands for each layer in both experiments.

sparser red regions in threshold-processed images. Due to its remote location from wells, both experiments showed comparable performance with substantially smaller cross-shaped sweep areas relative to the middle layer. Exp. B achieved a slightly larger sweep area and reduced vertical variation, yielding a sweep efficiency of 37.6%, compared to 31.5% in Exp. A. Oil saturation heatmap analysis revealed minimal inter-experiment differences, with average saturations of 55.62% for Exp. A and 52.17% for Exp. B. These results indicated that the MCCSF provided limited improvement within the lower reservoir layer.

In the bottom oil layer, effective utilization was challenging due to its significant distance from the wells, resulting in negligible differences between experimental groups. Both cases achieved limited sweep along upper high-permeability zones, though Exp. B exhibited lighter oil coloration (corresponding to more red dots in the thresholded images) and marginally higher sweep efficiency (14.1% vs. 12.9% in Exp. A). Edge-water invasion was evidenced through two key observations: one was the aqueous phase presence at lower-section boundaries (blue box region), and the other is the trend of lighter-colored oil sand was observed from the lower section boundaries toward the middle of the oil layer (green box region). This indicated that bottom water invasion partially supplemented displacement pressure and contributed to oil displacement. Oil saturation heatmaps revealed near-identical saturations, averaging 60.57% for Exp. A and 58.67% for Exp. B which indicated that MCCSF exhibited minimal effectiveness in this layer.

Comparative analysis revealed that MCCSF effectively mitigated the steam override and channeling phenomena in the principal oil layers (top, well, and middle layers), expanding the

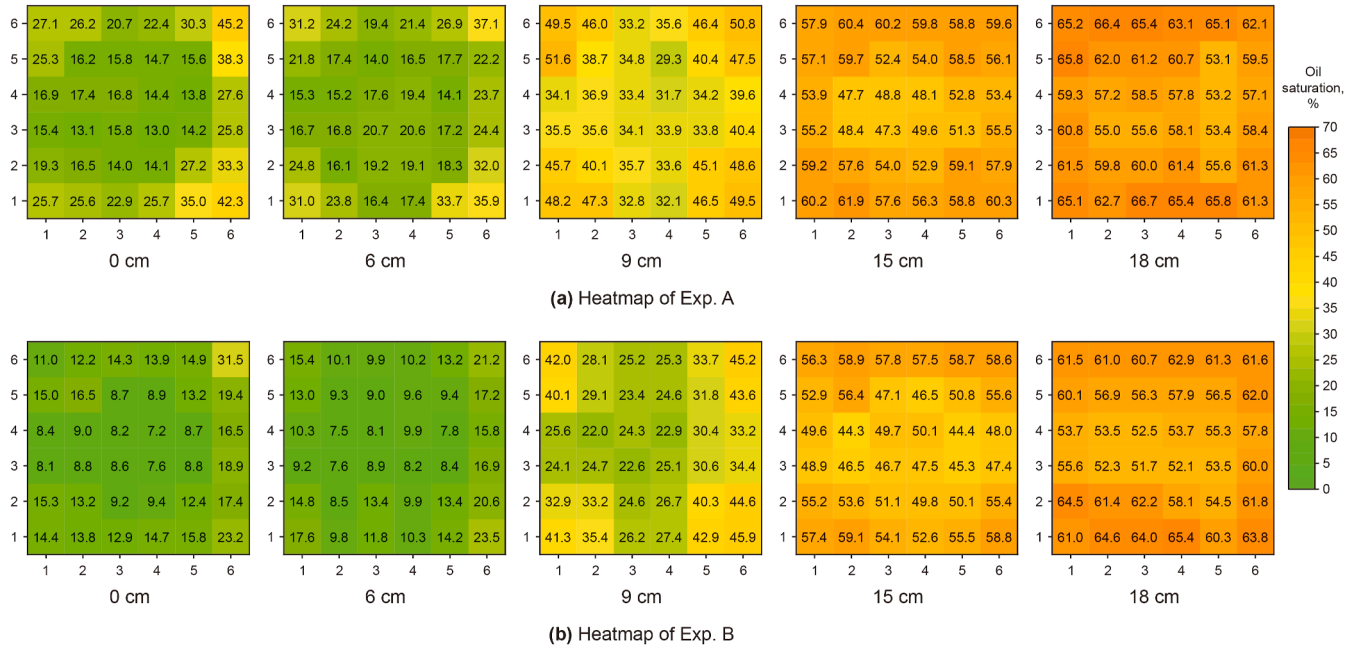

Fig. 16. Oil saturation heatmaps for Exps. A and B.

sweep area and enhancing the overall displacement efficiency. Additionally, it also improved the utilization of potential oil layers (lower and bottom layers) to some extent.

6. Conclusions

(1) A novel multi-external-aquifer 3D physical simulation method for edge-water reservoirs was developed and validated. This approach incorporated a derived similarity criterion number specifically for edge-water energy simulation, enabling accurate replication of production dynamics during recovery processes.

(2) Compared with PSF, MCCSF effectively prolonged the high-stable production period and delayed the onset of channeling. Throughout the production process, it achieved a higher peak oil production rate and oil–gas ratio, along with lower water cut and a slower water content increase. The final recovery factor reached 55.37%, which was 11.71% higher than that of PSF.

(3) The addition of multi-component significantly mitigated steam override, accelerated thermal connection between injection and production wells, and effectively reduced heat loss in the top oil layer. Simultaneously, it improved the imbalanced development of steam chamber caused by reservoir heterogeneity and dip angle. Compared with PSF, the overall steam chamber in MCCSF was more uniform and extensive, with a smaller temperature and sweep difference between higher and lower wells.

(4) MCCSF significantly enhanced the displacement effect of the middle and upper main reservoir layers. The sweep area of each layer was larger, and oil displacement efficiency across all thermal zones was notably improved. Compared with PSF, the average post-displacement oil saturation in the middle and upper layers was reduced by approximately 7%–10%. Meanwhile, utilization of the lower potential reservoir was also improved to a certain extent.

(5) For reservoirs with natural water aquifers, MCCSF offered significant advantages over PSF. The injected multi-component effectively maintained reservoir pressure, reduced steam partial pressure, and lowered the pressure difference between the reservoir and surrounding water aquifers, thereby effectively inhibiting water invasion.

CRediT authorship contribution statement

Qing-Jing Hong: Writing – original draft, Supervision, Methodology, Investigation, Data curation, Conceptualization. **Zhan-Xi Pang:** Writing – original draft, Supervision, Funding acquisition, Conceptualization. **Peng Tang:** Writing – original draft, Supervision. **Xiao-Hong Liu:** Supervision, Data curation. **Bo Wang:** Supervision, Data curation.

Conflict of interest

The authors declare no competing financial interest.

Acknowledgements

This study was supported by the National Natural Science Foundation of China (52574063) and the National Major Science and Technology Project of China (2025ZD1407704).

Appendix

Under elastic fluid drive theory, parameter solving was performed by constructing an equation that set actual elastic fluid production equal to the experimental elastic fluid production, with the main steps outlined below.

(1) Elastic productivity under reservoir conditions

During production, the decrease in formation pressure lowers pore fluid pressure, causing the fluids to expand. At the same time, the reduced fluid support allows the overburden pressure to compress the pore structure. Therefore, the total elastic liquid

production results from both fluid expansion and pore volume compression. The elastic liquid yield per unit pressure drop can be expressed as follows:

$$VL_1 = V_r\Delta p\left(C_f + \phi C_L\right) = V_r\Delta p\left[C_f + \phi(C_oS_o + C_wS_w)\right] \tag{A1}$$

Assuming that the reservoir is homogeneous, the dissolved gas in the heavy oil and the free gas in the reservoir are not considered, while ignoring the bound water in oil-bearing porous media. Then Eq. (A1) can be rewritten as

$$VL_1 = C_f\left(1 + \frac{aS_o}{S_w}\right)V_{r1}\Delta p + C_oV_{r1}\phi S_o\Delta p + C_w\frac{aV_{r1}S_o}{S_w}\phi S_w\Delta p \tag{A2}$$

Finally, when we know that the totally geological reserves is V_o, Eq. (A2) can be abbreviated as

$$VL_1 = V_o\Delta p\left(\frac{C_f(1 + aS_o)}{\phi S_o} + C_o + aC_w\right) \tag{A3}$$

(2) Elastic productivity under experimental conditions

Under the same conditions and assumptions, the elastic fluid production of the simulation model can be calculated as

$$\begin{aligned} VL_2 &= C_fV_{model}\Delta p + C_oV_{model}\phi S_o\Delta p + \sum_{i=1}^{m} C_fV_{pack}\Delta p \\ &+ \sum_{i=1}^{m} C_oV_{pack}\phi S_o\Delta p + \sum_{i=1}^{m} C_wV_{wi}\Delta p + \sum_{i=1}^{m} C_gV_{gi}\Delta p \\ &+ \sum_{j=m+1}^{n} C_fV_{pack}\Delta p + \sum_{j=m+1}^{n} C_wV_{pack}\phi\Delta p + \sum_{j=m+1}^{n} C_wV_{wj}\Delta p \\ &+ \sum_{j=m+1}^{n} C_gV_{g\varphi}\Delta p \end{aligned} \tag{A4}$$

(3) Solving process

Combining Eqs. (A1) and (A4), if we do not consider the compressibility of the rock and assume that the gas is ideal ($C_g = 1/p$) while replace the intermediate variables i and j with the variable k, the equation can be simplified as

$$\begin{aligned} &V_o(C_o + aC_w) - C_oV_{model}\phi S_o - mC_oV_{pack}\phi S_o \\ &\qquad - (n - m)C_wV_{pack}\phi = \sum_{k=1}^{n} C_wV_{wk} + \sum_{k=1}^{n}\frac{V_{gk}}{p_r} \end{aligned} \tag{A5}$$

In the left side of Eq. (A5), the volumes of the model, sand-pack, and the oil and water filled within can be directly calculated. The only parameter required conversion is the total oil content V_o, which should be scaled from the actual reservoir to the laboratory. As shown in Fig. 1, based on the field measured internal and external oil–water boundary distance, the actual oil-bearing cross-sectional area can be simplified to a trapezoid, the total oil content at laboratory scale can be calculated as

$$V_o = \left(HL_1{}^2 + HL_1L_2 + \frac{HL_1(L_3 - L_2)}{2}\right)\phi S_o \tag{A6}$$

Therefore, the left side of Eq. (A5) represents the known quantity of unreplaced fluid expansion which was abbreviate as V_S, so it can further simplify as

$$V_s = \sum_{k=1}^{n} C_wV_{wk} + \sum_{k=1}^{n}\frac{V_{gk}}{p_r} \tag{A7}$$

Then we can solve the volumes of water tank and gas tank in each layer through Eq. (A7), which contain $2n$ unknowns. Accordingly, an additional $(2n - 1)$ equations must be established to obtain a solvable system.

Firstly, to prevent external gas from entering the model during displacement, the volume of external water in each layer must be sufficient to ensure that the volume change of external gas during displacement is less than the volume of external water, which obtained n equations:

$$\begin{cases} V_{w1} + V_{g1} = \lambda\left(1 + \frac{p_r}{p_1}\right)V_{g1} & V_{w(m+1)} + V_{g(m+1)} = \lambda\left(1 + \frac{p_r}{p_1}\right)V_{g(m+1)} \\ \vdots & \vdots \\ V_{wi} + V_{gi} = \lambda\left(1 + \frac{p_r}{p_1}\right)V_{gi} & V_{wj} + V_{gj} = \lambda\left(1 + \frac{p_r}{p_1}\right)V_{gj} \\ \vdots & \vdots \\ V_{wm} + V_{gm} = \lambda\left(1 + \frac{p_r}{p_1}\right)V_{gm} & V_{wn} + V_{gn} = \lambda\left(1 + \frac{p_r}{p_1}\right)V_{gn} \end{cases} \tag{A8}$$

That is, we can simplify the system of Eq. (A8) to the following pattern:

$$V_{wk} = xV_{gk}, x = \lambda\left(1 + \frac{p_r}{p_1}\right) - 1 \tag{A9}$$

Secondarily, each gas tank connected to an aquifer layer was charged with an equimolar amount of nitrogen. Given the higher compressibility of gas compared to liquid, the energy of displaced edge-water was simulated by compressing the nitrogen in the tanks. This approach also enabled simulation of pressure differences among reservoir layers caused by vertical depth variations. A relationship between gas volume and pressure was thus established. By selecting the bottom external water aquifer as the reference reservoir pressure P_r, additional $(n - 1)$ equations can be derived based on the ideal gas law.

$$\begin{cases} \frac{P_rZ_{n-1}}{(P_r - \rho_ogH_{n-1}\cos\theta)Z_n} = \frac{V_{wg(n-1)}}{V_{wgn}} \\ \vdots \\ \frac{P_rZ_m}{(P_r - \rho_ogH_m\cos\theta)Z_n} = \frac{V_{ogm}}{V_{wgn}} \\ \vdots \\ \frac{P_rZ_1}{(P_r - \rho_ogH_1\cos\theta)Z_n} = \frac{V_{og1}}{V_{wgn}} \end{cases} \tag{A10}$$

That is, we can simplify the system of Eq. (A10) to the following pattern (for an ideal gas, $Z = 1$):

$$V_{gk} = y_kV_{gn},\ y_k = \frac{p_r}{p_r - \rho_ogH_k} \tag{A11}$$

Combining Eqs. (A7), (A9) and (A11), we can get the final Eq.

(A12) about solving V_{gn}, so that the volume of the water tank and the gas tank of each layer can be obtained

$$V_s = V_{gn} \sum_{k=1}^{n} y_k \left(x C_w + \frac{1}{p_r} \right) \tag{A12}$$

Finally, the similarity criterion number of simulated edge-water energy in 3D experiments was obtained by non-dimensionalizing the left-hand side of Eq. (A12):

$$\frac{V_s}{V_{gn}} = \sum_{k=1}^{n} y_k \left(x C_w + \frac{1}{p_r} \right) \tag{A13}$$

References

Afra, S., Nasr-El-Din, H.A., Socci, D., Cui, Z., 2018. Green phenolic amphiphile as a viscosity modifier and asphaltenes dispersant for heavy and extra-heavy oil. Fuel 220, 481–489. https://doi.org/10.1016/j.fuel.2018.01.111.

Bao, Y., Wang, J., Gates, I.D., 2016. On the physics of cyclic steam stimulation. Energy 115, 969–985. https://doi.org/10.1016/j.energy.2016.09.031.

Chen, M., Wang, Y., Chen, W., Ding, M., Zhang, Z., Zhang, C., Cui, S., 2023. Synthesis and evaluation of multi-aromatic ring copolymer as viscosity reducer for enhancing heavy oil recovery. Chem. Eng. J. 470. https://doi.org/10.1016/j.cej.2023.144220.

Dang, F., Li, S., Feng, S., 2025. Greening strategy for heavy oil thermal recovery assisted by environmental-friendly solvent dimethyl ether. Geoenergy Sci. Eng. 251. https://doi.org/10.1016/j.geoen.2025.213889.

Dong, L., 2012. Effect of vapour-liquid phase behaviour of steam-light hydrocarbon systems on steam assisted gravity drainage process for bitumen recovery. Fuel 95 (1), 159–168. https://doi.org/10.1016/j.fuel.2011.10.044.

Dong, X., Liu, H., Zhang, Z., Wang, C., 2014. The flow and heat transfer characteristics of multi-thermal fluid in horizontal wellbore coupled with flow in heavy oil reservoirs. J. Pet. Sci. Eng. 122, 56–68. https://doi.org/10.1016/j.petrol.2014.05.015.

Dong, X., Liu, H., Hou, J., Zhang, Z., Chen, Z., 2015. Multi-thermal fluid assisted gravity drainage process: A new improved-oil-recovery technique for thick heavy oil reservoir. J. Pet. Sci. Eng. 133, 1–11. https://doi.org/10.1016/j.petrol.2015.05.001.

Dong, X., Liu, H., Chen, Z., Wu, K., Lu, N., Zhang, Q., 2019. Enhanced oil recovery techniques for heavy oil and oilsands reservoirs after steam injection. Appl. Energy 239, 1190–1211. https://doi.org/10.1016/j.apenergy.2019.01.244.

Dong, X.-H., Jiang, X.-C., Zheng, W., Liu, H.-Q., Liu, R.-J., Wang, W.-C., Wang, T.-C., 2022a. Discussion on the sweep efficiency of hybrid steam-chemical process in heavy oil reservoirs: An experimental study. Pet. Sci. 19 (6), 2905–2921. https://doi.org/10.1016/j.petsci.2022.06.018.

Dong, X., Wang, J., Liu, H., Zeng, D., Zhang, Q., 2022b. Experimental investigation on the recovery performance and steam chamber expansion of multi-lateral well SAGD process. J. Pet. Sci. Eng. 214. https://doi.org/10.1016/j.petrol.2022.110597.

Dong, X., Liu, H., Tian, Y., Liu, S., Li, J., Jiang, L., Chen, Z., 2024. A new method to reduce shale barrier effect on sagd process: Experimental and numerical simulation studies using laboratory-scale model. SPE J. 29 (4), 2044–2059. https://doi.org/10.2118/218390-PA.

Elahi, S.M., Scott, C.E., Chen, Z., Pereira-Almao, P., 2019. In-situ upgrading and enhanced recovery of heavy oil from carbonate reservoirs using nano-catalysts: Upgrading reactions analysis. Fuel 252, 262–271. https://doi.org/10.1016/j.fuel.2019.04.094.

Guo, K., Li, H., Yu, Z., 2016. In-situ heavy and extra-heavy oil recovery: A review. Fuel 185, 886–902. https://doi.org/10.1016/j.fuel.2016.08.047.

Hong, Q., Pang, Z., Liu, X., Wang, B., Liu, D., Liao, H., Wang, L., 2025. Quantitative macro and micro analysis on enhanced oil recovery (EOR) mechanisms of multi-component composite steam flooding (MCCSF) based on image recognition algorithm. Geoenergy Sci. Eng. 249. https://doi.org/10.1016/j.geoen.2025.213766.

Jayasekera, A.J., Goodyear, S.G., 2000. The development of heavy oil fields in the United Kingdom Continental shelf: Past, present, and future. SPE Reserv. Eval. Eng. 3 (5), 371–379. https://doi.org/10.2118/65984-PA.

Jiang, H., Kang, W., Li, X., Peng, L., Yang, H., Li, Z., Turtabayev, S., 2021. Stabilization and performance of a novel viscoelastic N_2 foam for enhanced oil recovery. J. Mol. Liq. 337. https://doi.org/10.1016/j.molliq.2021.116609.

Jiang, H.Z., Yang, H.B., Ning, C.Y., Peng, L., Zhang, S.H., Chen, X., Kang, W.L., 2025. Amphiphilic polymer with ultra-high salt resistance and emulsification for enhanced oil recovery in heavy oil cold recovery production. Geoenergy Sci. Eng. 252. https://doi.org/10.1016/j.geoen.2025.213920.

Jiang, X., Dong, X., Xu, W., Liu, H., Chen, Z., 2024. Mathematical modeling for the production performance of cyclic multi-thermal fluid stimulation process in layered heavy oil reservoirs. Geoenergy Sci. Eng. 243. https://doi.org/10.1016/j.geoen.2024.213350.

Kar, T., Hascakir, B., 2021. Effect of solvent type on emulsion formation in steam and solvent-steam flooding processes for heavy oil recovery. Colloid Surf. A-Physicochem. Eng. Asp. 611. https://doi.org/10.1016/j.colsurfa.2020.125783.

Li, P., Wang, X., Zhang, Y., 2025. Thermal recovery of heavy oil reservoirs: Modeling of flow and heat transfer characteristics of superheated steam in full-length concentric dual-tubing wells. Geoenergy Sci. Eng. 244. https://doi.org/10.1016/j.geoen.2024.213432.

Li, Z., Lu, T., Tao, L., Li, B., Zhang, J., Li, J., 2011. CO_2 and viscosity breaker assisted steam huff and puff technology for horizontal wells in a super-heavy oil reservoir. Petrol. Explor. Dev. 38 (5), 600–605. https://doi.org/10.1016/S1876-3804(11)60059-1.

Lin, T., Song, H., Gu, Q., Xing, T., Tong, C., Zhang, W., Li, T., 2025. Case study: Multi-component thermal fluid technology to enhance production on thin-bedded heavy oil reservoir in Bohai Bay of China. Energy Rep. 13, 2245–2254. https://doi.org/10.1016/j.egyr.2025.01.071.

Lu, T., Xu, Z., Ban, X., Peng, D., Li, Z., 2022. Effect of flue gas on steam chamber expansion in steamflooding. SPE J. 27 (1), 399–409. https://doi.org/10.2118/206738-PA.

Lu, T., Li, Z., Du, L., 2024. Silica aerogel nanoparticle-stabilized flue gas foams for simultaneous CO_2 sequestration and enhanced heavy oil recovery. J. Clean. Prod. 434. https://doi.org/10.1016/j.jclepro.2023.140055.

Lyu, X., Liu, H., Pang, Z., Sun, Z., 2018. Visualized study of thermochemistry assisted steam flooding to improve oil recovery in heavy oil reservoir with glass micromodels. Fuel 218, 118–126. https://doi.org/10.1016/j.fuel.2018.01.007.

Mahood, H.B., Campbell, A.N., Sharif, A.O., Thorpe, R.B., 2016. Heat transfer measurement in a three-phase direct-contact condenser under flooding conditions. Appl. Therm. Eng. 95, 106–114. https://doi.org/10.1016/j.applthermaleng.2015.11.054.

McAuliffe, C.D., 1973. Crude-oil-water emulsions to improve fluid flow in an oil reservoir. J. Pet. Technol. 25 (6), 721–726. https://doi.org/10.2118/4370-pa.

Pang, Z., Wang, L., Wu, Z., Wang, X., 2019. An investigation into propagation behavior of the steam chamber during expanding-solvent SAGP (ES-SAGP). SPE J. 24 (2), 413–430. https://doi.org/10.2118/181331-PA.

Pang, Z., Jiang, Y., Wang, B., Cheng, G., Yu, X., 2020. Experiments and analysis on development methods for horizontal well cyclic steam stimulation in heavy oil reservoir with edge water. J. Pet. Sci. Eng. 188. https://doi.org/10.1016/j.petrol.2020.106948.

Pang, Z., Wang, L., Yin, F., Lyu, X., 2021. Steam chamber expanding processes and bottom water invading characteristics during steam flooding in heavy oil reservoirs. Energy 234. https://doi.org/10.1016/j.energy.2021.121214.

Pang, Z., Hong, Q., Liu, D., Wang, B., 2023. The macro and micro analysis on EOR mechanisms during steam and solvent thermal recovery in heavy oil reservoirs. Geoenergy Sci. Eng. 230. https://doi.org/10.1016/j.geoen.2023.212244.

Pang, Z.-X., Wang, Q.-H., Meng, Q., Wang, B., Liu, D., 2024. The mechanisms of thermal solidification agent promoting steam diversion in heavy oil reservoirs. Pet. Sci. 21 (3), 1902–1914. https://doi.org/10.1016/j.petsci.2024.01.001.

Perez-Perez, A., Mujica, M., Bogdanov, I., Hy-Billiot, J., 2016. A methodological analysis of the mechanisms associated with steam/solvent coinjection processes using dynamic gridding. SPE J. 21 (6), 2238–2249. https://doi.org/10.2118/169075-PA.

Pratama, R.A., Babadagli, T., 2022. A review of the mechanics of heavy-oil recovery by steam injection with chemical additives. J. Pet. Sci. Eng. 208. https://doi.org/10.1016/j.petrol.2021.109717.

She, Y., Mahardika, M.A., Hu, Y., Patmonoaji, A., Matsushita, S., Suekane, T., Nagatsu, Y., 2021. Three-dimensional visualization of the alkaline flooding process with in-situ emulsification for oil recovery in porous media. J. Pet. Sci. Eng. 202. https://doi.org/10.1016/j.petrol.2021.108519.

Soomro, N.A., 2025. Three-dimensional display of foam-driven oil displacement in porous materials. Int. J. Multiph. Flow 188. https://doi.org/10.1016/j.ijmultiphaseflow.2025.105221.

Sun, F., Li, C., Cheng, L., Huang, S., Zou, M., Sun, Q., Wu, X., 2017. Production performance analysis of heavy oil recovery by cyclic superheated steam stimulation. Energy 121, 356–371. https://doi.org/10.1016/j.energy.2016.12.132.

Sun, Q., Zhang, N., Liu, W., Li, B., Li, S., Bhusal, A., Li, Z., 2023. Insights into enhanced oil recovery by thermochemical fluid flooding for ultra-heavy reservoirs: An experimental study. Fuel 331. https://doi.org/10.1016/j.fuel.2022.125651.

Tian, J., Liu, H.Q., Pang, Z.X., 2017. A study of scaling 3D experiment and analysis on feasibility of SAGD process in high pressure environment. J. Pet. Sci. Eng. 150, 238–249. https://doi.org/10.1016/j.petrol.2016.11.036.

Wang, Y., Liu, H., Chen, Z., Wu, Z., Pang, Z., Dong, X., Chen, F., 2018. A visualized investigation on the mechanisms of anti-water coning process using nitrogen injection in horizontal wells. J. Pet. Sci. Eng. 166, 636–649. https://doi.org/10.1016/j.petrol.2018.03.083.

Wang, Y., Liu, P., Hua, D., Zhang, Z., Wang, C., Liu, P., Zhou, Y., 2025. Experimental and application research on sweep efficiency for non-condensable gases assisted vertical-horizontal steam drainage in extra-heavy reservoirs. Geoenergy Sci. Eng. 251. https://doi.org/10.1016/j.geoen.2025.213857.

Wei, J., Zhang, D., Yang, E., Shen, A., Zhou, R., 2024. Effect of foaming agent to CO_2 ratio on heavy oil recovery efficiency during steam stimulation. Geoenergy Sci. Eng. 242. https://doi.org/10.1016/j.geoen.2024.213206.

Xi, C., Qi, Z., Zhang, Y., Liu, T., Shen, D., Mu, H., Wang, H., 2019. CO_2 assisted steam flooding in late steam flooding in heavy oil reservoirs. Petrol. Explor. Dev. 46 (6), 1242–1250. https://doi.org/10.1016/s1876-3804(19)60277-6.

Yang, Z., Liu, X., Hua, Z., Ling, Y., Li, M., Lin, M., Dong, Z., 2015. Interfacial tension of CO_2 and crude oils under high pressure and temperature. Colloids Surf. A-Physicochem. Eng. Asp. 482, 611–616. https://doi.org/10.1016/j.colsurfa.2015.05.058.

Zhang, J., Wu, Y., Wang, C., Liu, P., Zhao, F., Xi, C., Liu, P., 2025. Synergistic improvement of sweep efficiency by urea in-situ decomposition and foaming agent in steam flooding for heavy oil reservoirs. Geoenergy Sci. Eng. 249. https://doi.org/10.1016/j.geoen.2025.213788.

Zhao, D.W., Wang, J., Gates, I.D., 2013. Optimized solvent-aided steam-flooding strategy for recovery of thin heavy oil reservoirs. Fuel 112, 50–59. https://doi.org/10.1016/j.fuel.2013.05.025.

Zou, B., Feng, H., Xia, X., Yu, T., Zheng, W., Xu, H., Cui, C., 2025. Study on the mechanism of CO_2 composite pressure flooding recovery enhancement in deep medium-low permeability heavy oil reservoirs. Geoenergy Sci. Eng. 249. https://doi.org/10.1016/j.geoen.2025.213764.